Mechanics of filled cellular materials

F. Ongaro [a], P. De Falco [a], E. Barbieri [a,*], N.M. Pugno [a,b,c,**]

[a] *School of Engineering and Materials Science, Queen Mary University of London, London, UK*
[b] *Laboratory of Bio-Inspired and Graphene Nanomechanics, Department of Civil, Environmental and Mechanical Engineering, University of Trento, Trento, Italy*
[c] *Center for Materials and Microsystems, Fondazione Bruno Kessler, Povo (Trento), Italy*

ABSTRACT

Many natural systems display a peculiar honeycomb structure at the microscale and numerous existing studies assume empty cells. In reality, and certainly for biological tissues, the internal volumes are instead filled with fluids, fibers or other bulk materials.

Inspired by these architectures, this paper presents a continuum model for composite cellular materials. A series of closely spaced independent linear-elastic springs approximates the filling material.

Firstly, finite element simulations performed on the microstructure and numerical homogenization demonstrate a convergence towards non-micro polarity, in contrast to classical empty materials. Secondly, theoretical homogenization, in its most general setting, confirms that the gradients of micro-rotations disappear in the continuum limit.

In addition, the resulting constitutive model remains isotropic, as for the non-filled cellular structures, and reconciles with existing studies where the filling material is absent.

Finally, the model is applied for estimating the mechanical properties of parenchyma tissues (carrots, apples and potatoes). The theory provides values for Young moduli reasonably close to the ones measured experimentally for turgid samples.

© 2016 Elsevier Ltd. All rights reserved.

1. Introduction

The use of cellular structures allows good mechanical properties at low weight. Nature adopts this advantageous strategy on numerous occasions in biological systems such as wood, bone, tooth, mollusk shells, crustaceans and many siliceous skeleton species like radiolarians, sea sponges and diatoms (Gordon et al., 2008; Neethirajan et al., 2009). Cellular structures have a diversity of functions but a fundamental one is mechanical, providing protection and support for the body. Natural cellular materials have been studied widely, the pioneering textbook by Gibson and Ashby (2001) and the exhaustive work by Gibson et al. (2010).

The factors influencing the mechanical properties of a cellular material are the apparent density, defined as the ratio between the density of the cellular solid and the density of the material, the internal architecture and the material properties of the microstructure. In its most sophisticated form, natural cellular materials are even able to adapt their architectures to changing mechanical environments (Fratzl and Weinkamer, 2007; 2011). One example is the combination of dense and strong fibre-composite outer faces and an inner foam-like core in the leaves of monocotyledon plants, like irises and maize (Gibson, 2012), which better resist bending and buckling. The lightweight core, in particular, is a simple plant tissue, known as parenchyma (Gibson, 2012; Gibson

---

* Corresponding author at: School of Engineering and Materials Science, Queen Mary University of London, London, UK. Tel.: +4402078826310.
** Corresponding author at: Laboratory of Bio-Inspired and Graphene Nanomechanics, Department of Civil, Environmental and Mechanical Engineering, University of Trento, Trento, Italy.
E-mail addresses: f.ongaro@qmul.ac.uk (F. Ongaro), p.defalco@qmul.ac.uk (P. De Falco), e.barbieri@qmul.ac.uk (E. Barbieri), nicola.pugno@unitn.it (N.M. Pugno).
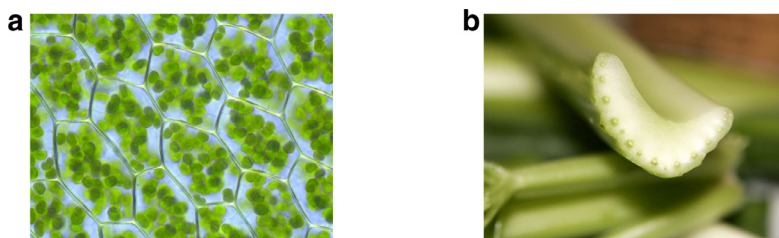
Fig. 1. (a) Parenchyma tissue from the moss Plagiomnium Affine, (b) Natural tubular structures: celery cross section.

et al., 2010; Bruce, 2003; Warner et al., 2000; Georget et al., 2003) made up of thin-walled polyhedral cells filled by liquid and, notwithstanding its low relative density and low mechanical properties, can significantly improve the resistance of the leaf. Similar composite solutions are found in the natural tubular structures, like plant stems or animal quills. In these systems, the inner honeycomb or foam-like core behaves like an elastic foundation supporting the dense outer cylindrical shell and makes it more performant (Gibson, 2005; Dawson and Gibson, 2007), Fig. 1.

It is well known (Gibson and Ashby, 2001) that the main problem with cellular materials is to extract an equivalent continuum model. In fact, the formulation of a continuum model is hindered by two types of difficulties: the spatial variability of size and morphology of the microscopic architecture, on one side, and the crucial passage from the microscopic discrete description to the coarse continuous one, on the other. The typical approach to the continuum modeling of cellular materials includes the assumption of periodicity and the selection of a representative volume element (RVE). Moreover, it necessitates the application of micro-macro relationships in terms of forces and displacements and energy equivalence concepts. Furthermore, the material properties are typically assumed to be as simple as possible, for example linear-elastic and isotropic (Altenbach and Oechsner, 2010).

Various authors extensively studied cellular materials. Among them, Gibson and Ashby (2001), Gibson et al. (2010), Gibson (1989), Gibson et al. (1982) obtained simple power-law relations between the density of a wide range of honeycombs and foams and their mechanical properties, studying regular cellular structures and assuming a prevalent mode of deformation and failure. Other authors, like Chen et al. (1998), Davini and Ongaro (2011), Kumar and McDowell (2004), Warren and Byskov (2002), Wang and Stronge (1999), Dos Reis and Ganghoffer (2012), Pugno (2006), Chen and Pugno (2012, 2011), Gonella and Ruzzene (2008) focused on the passage from discrete to continuum and deduced the constitutive model for the in-plane deformation of various two-dimensional microstructures (triangle, hexagonal, rectangular, square, re-entrant or mixed lattices). (Chen et al., 1998) and (Kumar and McDowell, 2004), in particular, considered an infinite arrangement of equal cells and derived a continuum model (a micropolar continuum) introducing asymptotic Taylor expansion of the displacement and rotation fields in the strain energy of the system. Applying the principles of structural analysis to the representative volume element, Warren and Byskov

(2002) and Wang and Stronge (1999) obtained the equivalent (micropolar) constitutive equations associated with the homogenized continuum model of the discrete lattice. Dos Reis and Ganghoffer (2012) elaborated a variant of the asymptotic homogenization technique introduced by Caillerie et al. (2006) and calculated the effective behavior of a 2D square and hexagonal lattices through the analysis of discrete sums. In accordance with the papers quoted above, the adopted technique leads to a micropolar equivalent continuum. Adopting the viewpoint of homogenization theory, Davini and Ongaro (2011) constructed a continuum model for the in-plane deformations of a honeycomb material from general theorems of Γ-convergence. Differently from (Chen et al., 1998), (Kumar and McDowell, 2004), (Warren and Byskov, 2002), (Wang and Stronge, 1999), it emerges that the limit model is a pseudo-polar continuum, that is a material that can undergo applied distributed couples without developing couple stresses. Finally, Gonella and Ruzzene (2008) investigated the equivalent in-plane properties of a square, hexagonal and re-entrant lattices through homogenization techniques. In particular, the adopted homogenization approach yields the continuum set of partial differential equations associated with their equivalent continuum model. The assumption of no concentrated couples acting to the structure in conjunction with the appropriate elasticity equations lead to the equivalent Young's moduli and Poisson's ratios.

In the literature, few investigations concern the characterization of cellular materials having filled cells. Niklas (1989), for example, dealt with the mechanical behavior of plant tissues and provided an analytical description of the influence of the turgor pressure on the effective stiffness. Georget et al. (2003) considered the stiffness of the carrot tissue as a function of the turgor pressure and the mechanical properties of the cell walls. By modeling the tissue as a fluid-filled foam, the authors found good agreement between their predictions and the experimental values. Warner et al. (2000), which goes in this direction, investigated a range of deformation mechanisms of closed-cell cellular solids, unfilled and filled with liquid, to characterize elasticity and failure in foods. In particular, above a critical strain, it emerged that the filling liquid forced the walls to stretch rather than to bend as they do when a dry cellular solid is deformed. In the context of sandwich panels, Burlayenko and Sadowski (2010) presented a finite element-based technique to evaluate the structural performance of sandwich plates with a hexagonal honeycomb core made of aluminium alloy and filled with PVC foam.
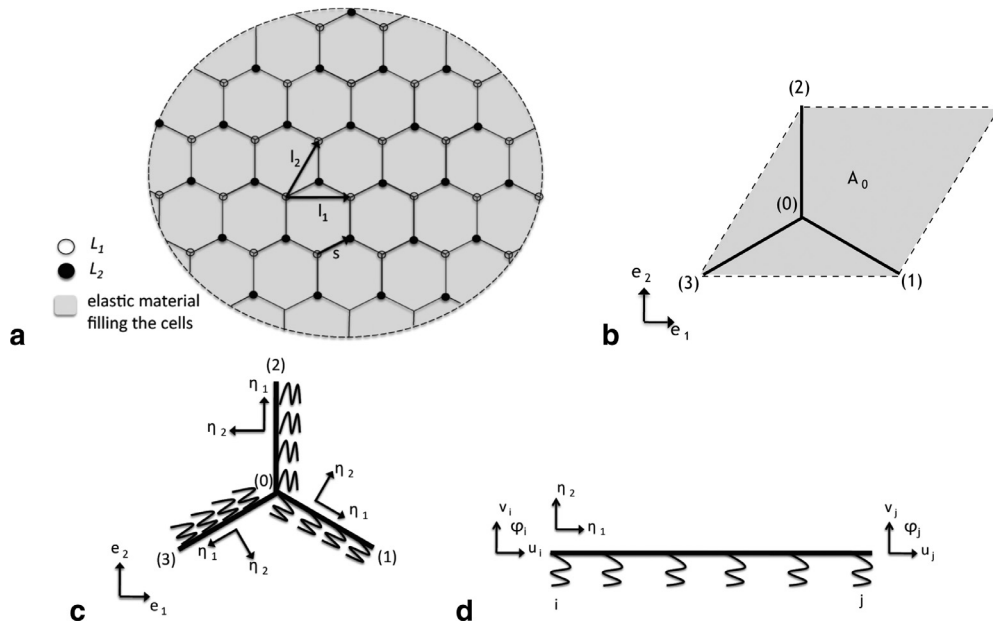
Fig. 2. (a) The hexagonal microstructure, (b) The unit cell, (c) The triplet of elastic beams, (d) The beam on Winkler elastic foundation: degrees of freedom in the local reference system.

Specifically, the investigation suggests that the effective elastic properties of a honeycomb sandwich panel are improved by the presence of the filling PVC foam. The in-plane crush response and energy absorption of a circular cell honeycomb filled with PDMS elastomer is studied in (D'Mello and Waas, 2013). It emerged an increase in the load carrying capacity and an improvement in the energy absorption capability due to the presence of the filling material. More recently, Guiducci et al. (2014) investigated the mechanics of a diamond-shaped honeycomb internally pressurized by a fluid phase. The authors proposed a theoretical model based on the Born model, as well as a finite element-based analysis to study the consequences of the pressure within the cells. Two different effects emerged: a marked change in the lattice's geometry and an improvement in the load-bearing capacity of the material.

This paper, inspired by the aforementioned high efficiency of the composite structures in nature, deals with the mechanical behavior of a 2D composite cellular material subjected to in-plane loads. In particular, the analysis focuses on a honeycomb-like microstructure having the cells filled by a generic elastic material, represented by a sequence of beams on Winkler elastic foundation. The paper proceeds as follows. Firstly, Section 2 describes the equivalence between the hybrid system continuum-springs and the biphasic continuum-continuum. Numerical simulations on a single composite cell show the implications of the modeling approach based on the Winkler model. Then, Section 3 focuses on the passage from the discrete description to the continuum one and the effective constitutive equations and elastic moduli are derived. Some considerations about the influence of the microstructure parameters on the overall elastic constants are reported in Section 4, as well as a comparison between our model and those available in literature. The results of the comparison

between numerical and theoretical homogenization are also provided. Finally, Section 5 illustrates the application of the theoretical model to the biological parenchyma tissue of carrot, apple and potato.

To the authors' best knowledge, this is the first time to report such results. In fact, the beam on Winkler foundation model has never been applied to represent the microstructure of a 2D composite cellular material.

2. Equivalence between the biphasic continuum and the hybrid system continuum - springs

A sequence of elastic beams of length ℓ, forming a periodic array of hexagonal cells (Fig. 2a), simulates a cellular composite material having a hexagonal microstructure. The Euler-Bernoulli beam on Winkler foundation model simulates each beam. Specifically, a series of closely spaced independent linear elastic springs of stiffness k_w, the Winkler foundation constant per unit width, approximate the elastic material filling the cells (Fig. 2c and d).

It should be noted that modeling the material within the cells by a Winkler foundation is a simplification aimed at obtaining a more mathematically tractable problem. However, this could affect the prediction ability of the proposed model.

Numerical simulations on a computational model of a single composite cell provide the right value of the k_w constant. Also, the Finite Element (FE) simulations illustrate the implications of the modeling approach based on the Winkler model, Figs. 5 and 6, as well as the deformation mechanisms of the system continuum-springs, Fig. 7. As Fig. 3 shows, two different configurations are considered. In the first one, Fig. 3a, the filling material is represented by the Winkler foundation while in the second, Fig. 3b,
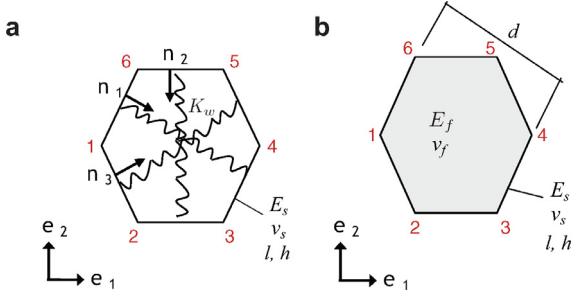
Fig. 3. Equivalence between the elastic moduli of the filling material and corresponding spring. (a) Filling material as a Winkler foundation, (b) Filling material as a classical continuum.

by a classical continuum having Young's modulus E_f and Poisson's ratio of v_f.

First of all, let us focus on a suitable relation between E_f, v_f and the Winkler foundation constant k_w. As Fig. 3 shows, the elastic energy of the cell, W_c, is obtained by summing the contribution of the walls, W_w, and of the filling material, W_f:

$$W_c = W_w + W_f. \tag{1}$$

Assuming that the elastic energy of the cell walls is the same of the elastic beams, Fig. 3a, and in the case of filling material as a classical continuum, Fig. 3b, the equivalence

$$W_{w, beams} \equiv W_{w, continuum} \tag{2}$$

takes the form

$$W_{f, Winkler} \equiv W_{f, continuum}. \tag{3}$$

Note that in (2) and (3) $W_{w, beams}$, $W_{f, Winkler}$ and $W_{w, continuum}$, $W_{f, continuum}$ stand for the elastic energies of the cell walls and of the filling material in the cases of Winkler foundation model and of continuum model, respectively. In particular, $W_{f, Winkler}$ derives from the elastic energies of the three sets of springs in the directions $\mathbf{n}_1$, $\mathbf{n}_2$, $\mathbf{n}_3$ (Fig. 3a):

$$W_{f, Winkler} = \left(\sum_{i=1}^{3} \frac{1}{2} \, \Delta \, \mathbf{U}_i^T \cdot \mathbf{K}_w \Delta \, \mathbf{U}_i \right) b, \tag{4}$$

with $\Delta \mathbf{U}_i$ the elongation of the springs in the $\mathbf{n}_i$ direction, b the width,

$$\mathbf{K}_w = \begin{bmatrix} K_w & 0 \\ 0 & K_w \end{bmatrix} \tag{5}$$

the stiffness matrix of the elastic foundation, $K_w = k_w \ell$ the Winkler constant and ℓ the length of the walls. It should be noted that in Fig. 3a, for ease of reading, the series of springs are represented by three single springs having stiffness K_w in the directions $\mathbf{n}_1$, $\mathbf{n}_2$, $\mathbf{n}_3$.

Moreover,

$$W_{f, continuum} = \frac{1}{2} \int_V \boldsymbol{\sigma}_f^T \boldsymbol{\epsilon}_f \, dV = \frac{1}{2} \int_V \boldsymbol{\epsilon}_f^T \mathbf{C}_f \boldsymbol{\epsilon}_f \, dV, \tag{6}$$

been $V = A b$ and $A = \dfrac{3\sqrt{3}\ell^2}{2}$, respectively, the volume and the area of the cell, $\boldsymbol{\epsilon}_f$, $\boldsymbol{\sigma}_f$, $\mathbf{C}_f$, in turn, the strain tensor,

stress tensor and elastic modulus tensor of the material within the cell, satisfying the relation

$$\boldsymbol{\sigma}_f = \mathbf{C}_f \boldsymbol{\epsilon}_f, \tag{7}$$

or

$$\begin{bmatrix} \sigma_{11} \\ \sigma_{22} \\ \sigma_{12} \end{bmatrix} = \frac{E_f}{(1+v_f)(1-2v_f)}$$

$$\times \begin{bmatrix} (1-v_f) & v_f & 0 \\ v_f & (1-v_f) & 0 \\ 0 & 0 & (1-2v_f) \end{bmatrix}. \tag{8}$$

From classical continuum mechanics, the deformation of the filling material in the generic $\mathbf{n}_i$ direction is (Fig. 3)

$$\mathbf{n}_i^T \boldsymbol{\epsilon}_f \mathbf{n}_i = \frac{\Delta d_i}{d}, \qquad i = 1, 2, 3 \tag{9}$$

where Δd_i is the elongation in the $\mathbf{n}_i$ direction and $d = \sqrt{3}\ell$. The assumption

$$\Delta U_i = \Delta d_i, \qquad i = 1, 2, 3 \tag{10}$$

leads to

$$\mathbf{n}_i^T \boldsymbol{\epsilon}_f \mathbf{n}_i = \frac{\Delta U_i}{d} \rightarrow \Delta U_i = (\mathbf{n}_i^T \boldsymbol{\epsilon}_f \mathbf{n}_i)d, \qquad i = 1, 2, 3. \tag{11}$$

Substituting (11) into (3) gives

$$\sum_{i=1}^{3} \frac{1}{2} d(\mathbf{n}_i^T \boldsymbol{\epsilon}_f \mathbf{n}_i)^T \mathbf{n}_i^T \mathbf{K}_w \mathbf{n}_i (\mathbf{n}_i^T \boldsymbol{\epsilon}_f \mathbf{n}_i) \, d = \frac{1}{2} \left(\boldsymbol{\epsilon}_f^T \mathbf{C}_f \boldsymbol{\epsilon}_f \right) A. \tag{12}$$

Considering the deformation states

$$\boldsymbol{\epsilon}_f = \begin{bmatrix} 1 \\ 0 \\ 0 \end{bmatrix}, \qquad \boldsymbol{\epsilon}_f = \begin{bmatrix} 0 \\ 1 \\ 0 \end{bmatrix}, \qquad \boldsymbol{\epsilon}_f = \begin{bmatrix} 0 \\ 0 \\ 1 \end{bmatrix} \tag{13}$$

and substituting, in turn, (13) into (12) provides

$$\frac{3\sqrt{3}\, K_w}{8} = \frac{E_f(v_f - 1)}{2(2v_f - 1)(v_f + 1)},$$

$$\frac{\sqrt{3}\, K_w}{2} = \frac{E_f}{(v_f + 1)}. \tag{14}$$

Accordingly,

$$v_f = 0.25, \qquad E_f = \frac{5\sqrt{3}\, K_w}{8} \tag{15}$$

and, in the case of isotropic filling material, the shear modulus takes the form

$$G_f = \frac{E_f}{2(v_f + 1)} = \frac{\sqrt{3}\, K_w}{4}. \tag{16}$$

As clearly seen, this theory leads to a fixed Poisson's ratio, known result from the Spring Network Theory (Alzebdeh and Ostoja-Starzewski, 1999), (Ostoja-Starzewski, 2002).

Regarding the cell considered in the numerical simulations, $K_w = 10^{-1}$ GPa. The walls, assumed to be isotropic linear elastic, have Young's modulus $E_s = 79$ GPa, Poisson's ratio $v_s = 0.35$, thickness $h = 1$ mm, length $\ell = 10$ mm and unitary width. As more fully described in Section 4, each node has three degrees of freedom: two in-plane displacements and the rotational component. The three loading

states analyzed, Fig. 4, are simulated by applying uniaxial forces of the same intensity at the boundary nodes. Specifically, forces of intensity, 10^{-3} N in the directions $\mathbf{e}_1$, Fig. 4a, and $\mathbf{e}_2$, Fig. 4b, and shear forces of 10^{-5} N, Fig. 4c are adopted. As Fig. 4 shows, constrained nodes are introduced to avoid rigid body motions that could lead to an erroneous comparison between the deformed configurations of the two considered models.

The results of the analysis, summarized in Figs. 5 and 6, illustrate that the predictions of the Winkler foundation model are in accordance with those obtained in the case of filling material as a classical continuum.

Specifically, in terms of the horizontal and vertical displacements of the nodes, U_X and U_Y respectively, the difference between the two estimates, ΔU_X and ΔU_Y, is generally $1-3\%$ (Fig. 6).

Furthermore, in the case of uniaxial compression in the $\mathbf{e}_1$ direction it emerges an higher difference between the horizontal displacements of node 1 predicted by the two models, Fig. 6a. This is due to the limitations of the Winkler foundation model, where the elastic springs only connect two opposite beams, 1-2 and 4-5, 6-1 and 3-4 (Fig. 3a). The beams 1-2 and 3-4, 6–1 and 4-5 that, in reality, are coupled by the presence of the filling material, in the Winkler model are not connected. However, in view of Figs. 5a and 6a, the consequences of this simplification slightly affect the prediction ability of the proposed model.

Similarly, in the case of vertical compression, Fig. 4b, the high values of ΔU_X and ΔU_Y at nodes 1, 4 are related to the limitations induced by the Winkler model.

Regarding Fig. 6c, the same considerations apply. That is to say, the missing influence of the filling material on the beams 1-6 and 4-5 provides an high value of ΔU_X at the nodes 5 and 6.

As a conclusion, it can be said that the analysis reveals the validity of the modeling approach based on the Winkler model, notwithstanding the simplifications introduced.

3. Theoretical model and homogenization of the continuum - springs system

3.1. Geometry and energy of the discrete problem

3.1.1. Geometric description

The hexagonal microstructure of the composite material considered here can be described as the union of two simple Bravais lattices,

$$L_1(\ell) = \left\{ \mathbf{x} \in \mathbb{R}^2 : \mathbf{x} = n^1 \mathbf{l}_1 + n^2 \mathbf{l}_2 \,, \text{with } (n^1, n^2) \in \mathbb{Z}^2 \right\},$$
$$L_2(\ell) = \mathbf{s} + L_1(\ell), \qquad (17)$$

simply shifted with respect to each other by the *shift vector* $\mathbf{s}$. In Cartesian coordinates,

$$\mathbf{s} = (\sqrt{3}\,\ell/2,\ \ell/2), \quad \mathbf{l}_1 = (\sqrt{3}\,\ell,\ 0), \quad \mathbf{l}_2 = (\sqrt{3}\,\ell/2,\ 3\,\ell/2) \qquad (18)$$

describe the *shift vector* and the *lattice vectors*, $\mathbf{l}_1$ and $\mathbf{l}_2$ (Fig. 2a).

The lattice vectors and the shift vector define the *unit cell* of the periodic array (Fig. 2b), which is composed by the central node (0) and the three external nodes (1), (2),
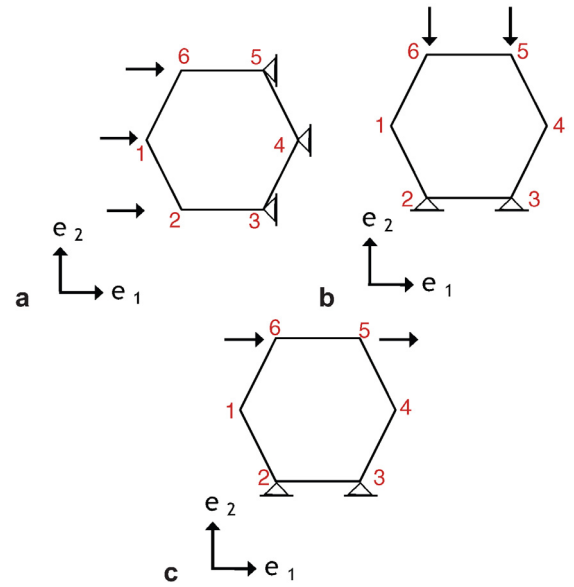

Fig. 4. Finite element implementation of the composite cell, the load conditions. (a) Uniaxial compression in the $\mathbf{e}_1$ direction, (b) Uniaxial compression in the $\mathbf{e}_2$ direction, (c) Shear forces.

(3), linked by the elastic beams (0)-(1), (0)-(2) and (0)-(3), represented by the vectors $\mathbf{b}_1 = \mathbf{l}_1 - \mathbf{s}$, $\mathbf{b}_2 = \mathbf{l}_2 - \mathbf{s}$, $\mathbf{b}_3 = -\mathbf{s}$. The area of the unit cell is $A_0 = |\mathbf{l}_1 \times \mathbf{l}_2| = \frac{3\sqrt{3}}{2}\,\ell^2$.

The analysis of the representative cell of the microstructure provides the strain energy density of the discrete structure. Its continuum approximation is then the consequence of a particular assumption.

3.1.2. The hybrid system: Euler–Bernoulli beam on Winkler foundation

Let us consider the beam element in the 2D space. Neglecting, for simplicity, the second order effects and the shear deformability, it is subjected to bending and axial deformation. The hypothesis of two-dimensional structure also prevents the possibility of torsion and bending in the normal plane. The fields of axial and transverse displacement of its axis and the rotation of its section describe the kinematics of a generic element. In a *global reference system*, defined by the unit orthonormal vectors $\mathbf{e}_1$ and $\mathbf{e}_2$ with origin in O and by the Cartesian coordinate system $\mathbf{X} = (X, Y)^T$, the configuration of the eth structural element is known by specifying the coordinates of its end nodes I and J. According to the kinematics of the incident beams, each node has three degrees of freedom, two translations and one rotation (Fig. 2d). Finally, forces arbitrarily oriented and couples act at the extreme nodes of each beam.

To analyze the generic structural element is more convenient to use a *local reference system*, specific to the considered beam and closely dependent to its geometry. Such reference consists of two orthonormal unit vectors (η^e_1, η^e_2), Figs. 2c and d, and a coordinate system (x, y). Note that, in the sequel, the extreme nodes of the beam in the local notation are denoted by the indices i and j, Fig. 2d.
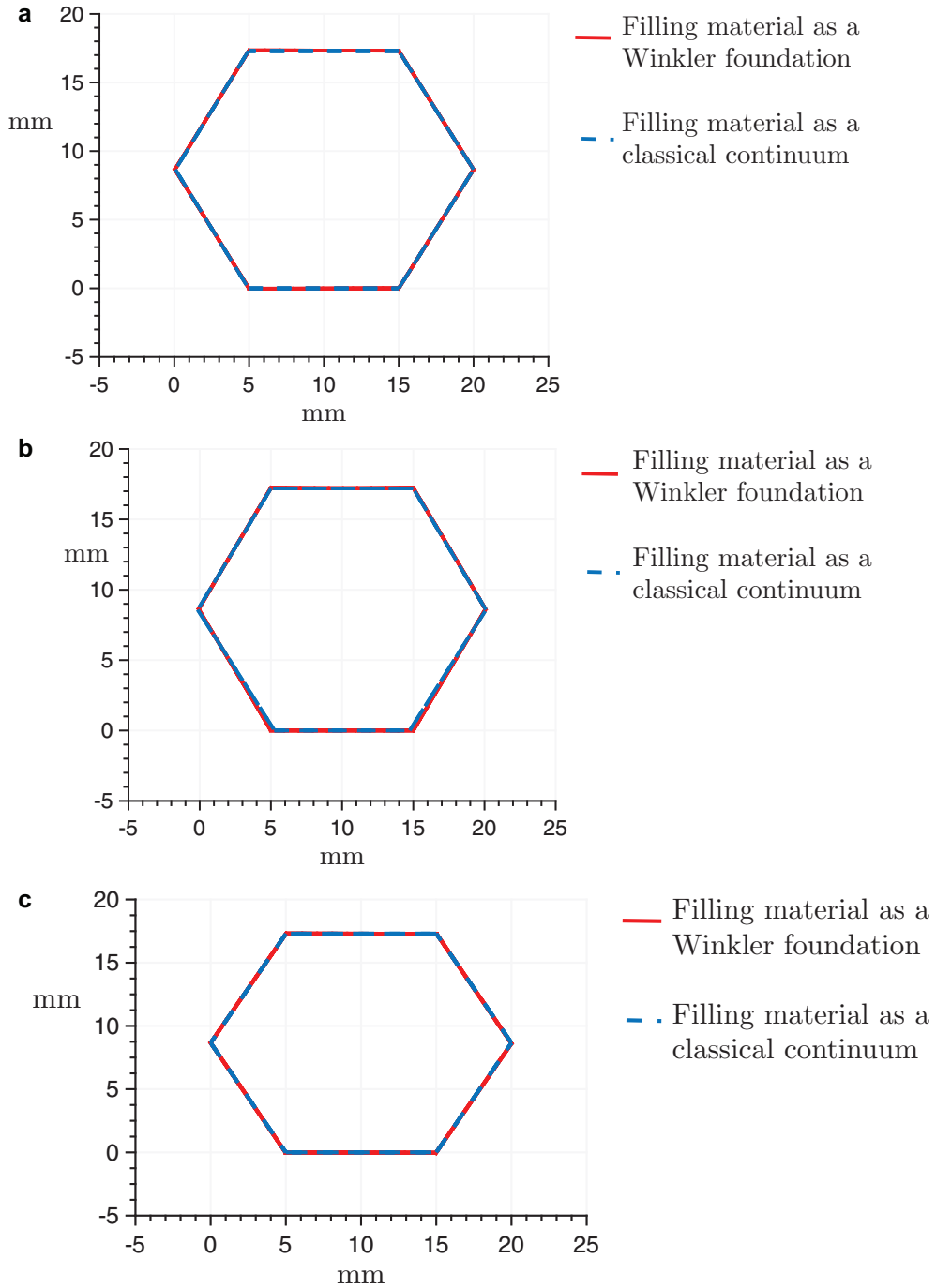
Fig. 5. Filling material as a Winkler foundation vs. filling material as a classical continuum, superposition of the deformed configurations in the case of (a) Uniaxial compression in the $\mathbf{e}_1$ direction with forces of 10^{-3} N, (b) Uniaxial compression in the $\mathbf{e}_2$ direction with forces of 10^{-3} N, (c) Shear forces of 10^{-5} N, and with $K_w = 10^{-1}$ Pa, $E_s = 79$ GPa, $\nu_s = 0.35$, $h = 1$ mm, $l = 10$ mm.
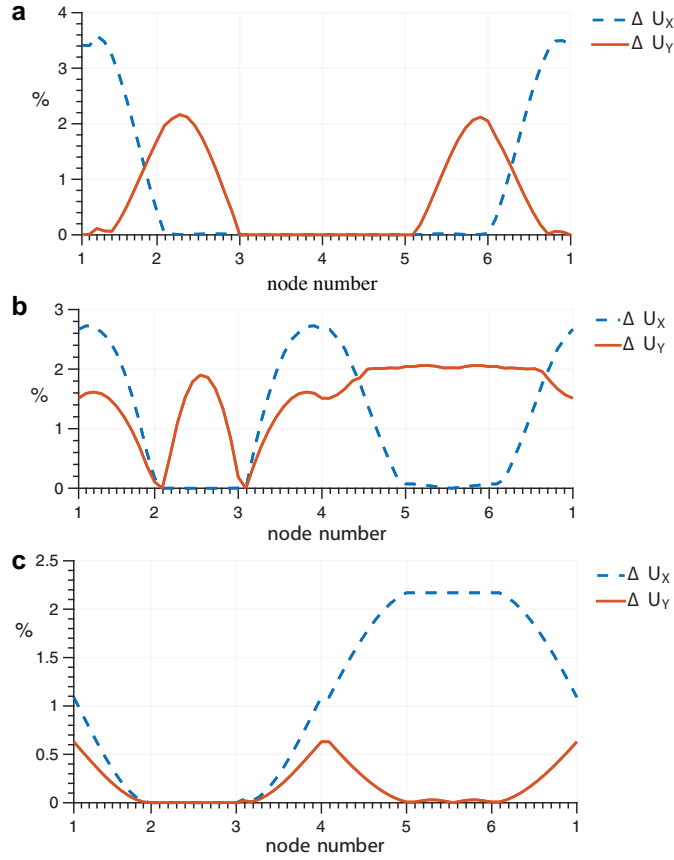
Fig. 6. Filling material as a Winkler foundation vs. filling material as a classical continuum, comparison between the nodal displacements in the case of (a) Uniaxial compression in the $\mathbf{e}_1$ direction with forces of 10^{-3} N, (b) Uniaxial compression in the $\mathbf{e}_2$ direction with forces of 10^{-3} N, (c) Shear forces of 10^{-5} N, and with $K_w = 10^{-1}$ Pa, $E_s = 79$ GPa, $\nu_s = 0.35$, $h = 1$ mm, $l = 10$ mm.

The introduction of the local reference system allows us to define more easily the *stiffness matrices* $\mathbf{k}_b^e$ and $\mathbf{k}_{wf}^e$ that are, respectively, the stiffness matrix of the classical elastic beam and of the Winkler foundation (Janco, 2010), denoted by lowercase letters since they are expressed in the local reference. Their components are

with $K_w = k_w \ell$, k_w the Winkler foundation constant per unit width, $C_\ell = \frac{E_s h}{1 - \nu_s^2}$ and $D_\ell = \frac{E_s h^3}{12(1 - \nu_s^2)}$, respectively, the tensile and bending stiffness (per unit width) of the beams, E_s, ν_s, h and ℓ, in turn, the Young's modulus, Poisson's ratio, thickness and length of the cell walls.

$$\mathbf{k}_b^e = \begin{bmatrix} C_\ell/\ell & 0 & 0 & -C_\ell/\ell & 0 & 0 \\ 0 & 12D_\ell/\ell^3 & 6D_\ell/\ell^2 & 0 & -12D_\ell/\ell^3 & 6D_\ell/\ell^2 \\ 0 & 6D_\ell/\ell^2 & 4D_\ell/\ell & 0 & -6D_\ell/\ell^2 & 2D_\ell/\ell \\ -C_\ell/\ell & 0 & 0 & C_\ell/\ell & 0 & 0 \\ 0 & -12D_\ell/\ell^3 & -6D_\ell/\ell^2 & 0 & 12D_\ell/\ell^3 & -6D_\ell/\ell^2 \\ 0 & 6D_\ell/\ell^2 & 2D_\ell/\ell & 0 & -6D_\ell/\ell^2 & 4D_\ell/\ell \end{bmatrix} \tag{19}$$

and

$$\mathbf{k}_{wf}^e = \begin{bmatrix} 0 & 0 & 0 & 0 & 0 & 0 \\ 0 & 13K_w/35 & 11K_w\ell/210 & 0 & 9K_w/70 & -13K_w\ell/420 \\ 0 & 11K_w\ell/210 & K_w\ell^2/105 & 0 & 13K_w\ell/420 & -K_w\ell^2/140 \\ 0 & 0 & 0 & 0 & 0 & 0 \\ 0 & 9K_w/70 & 13K_w\ell/420 & 0 & 13K_w/35 & -11K_w\ell/210 \\ 0 & -13K_w\ell/420 & -K_w\ell^2/140 & 0 & -11K_w\ell/210 & K_w\ell^2/105 \end{bmatrix}, \tag{20}$$

The *elastic energy* of each beam, obtained by superposition principle due to the assumption of linear elastic beam, is

$$w^e = \frac{1}{2}(\mathbf{u}^e)^T \cdot \mathbf{k}_b^e \mathbf{u}^e + \frac{1}{2}\left(\frac{1}{2}(\boldsymbol{\Delta}\,\mathbf{u}^{e,a})^T \cdot \mathbf{k}_{wf}^e \boldsymbol{\Delta}\,\mathbf{u}^{e,a}\right)$$
$$+ \frac{1}{2}\left(\frac{1}{2}(\boldsymbol{\Delta}\,\mathbf{u}^{e,b})^T \cdot \mathbf{k}_{wf}^e \boldsymbol{\Delta}\,\mathbf{u}^{e,b}\right), \tag{21}$$

where $\mathbf{u}^e = [\mathbf{u}_i, \mathbf{u}_j]^T = [u_i, v_i, \varphi_i, u_j, v_j, \varphi_j]^T$ is the generalized *vector of nodal displacement expressed in the local reference* and

$$\boldsymbol{\Delta}\,\mathbf{u}^{e,a} = \left[\boldsymbol{\Delta}\,\mathbf{u}_i^a, \boldsymbol{\Delta}\,\mathbf{u}_j^a\right]^T$$
$$= \left[\Delta u_i^a, \Delta v_i^a, \Delta \varphi_i^a, \Delta u_j^a, \Delta v_j^a, \Delta \varphi_j^a\right]^T, \tag{22}$$

$$\boldsymbol{\Delta}\,\mathbf{u}^{e,b} = \left[\boldsymbol{\Delta}\,\mathbf{u}_i^b, \boldsymbol{\Delta}\,\mathbf{u}_j^b\right]^T$$
$$= \left[\Delta u_i^b, \Delta v_i^b, \Delta \varphi_i^b, \Delta u_j^b, \Delta v_j^b, \Delta \varphi_j^b\right]^T \tag{23}$$

is the elongation of the springs a, the first, and of the springs b, the second (Figs. 8 and 9). In particular, the springs a and the springs b connect each beam with the opposite one in the $-\boldsymbol{\eta}_2^e$ and $+\boldsymbol{\eta}_2^e$ direction, respectively. See Appendix A for further details. Note that the factor 1/2 in the second and third term of (21), is due to the fact that each spring is shared by two opposite beams and contribute only half of its strain energy to the unit cell.

In the local reference, the forces and couples acting at the end of each beam are

$$\mathbf{f}^e = \mathbf{k}_b^e \mathbf{u}^e + \mathbf{k}_{wf}^e \boldsymbol{\Delta}\,\mathbf{u}^{e,a} + \mathbf{k}_{wf}^e \boldsymbol{\Delta}\,\mathbf{u}^{e,b}, \tag{24}$$

with $\mathbf{f}^e = [\mathbf{f}_i, \mathbf{f}_j]^T = [f_{xi}, f_{yi}, m_i, f_{xj}, f_{yj}, m_j]^T$ the *vector of nodal forces and couples* and $\mathbf{u}^e$, $\boldsymbol{\Delta}\,\mathbf{u}^{e,\,a}$, $\boldsymbol{\Delta}\,\mathbf{u}^{e,\,b}$, $\mathbf{k}_b^e$ and $\mathbf{k}_{wf}^e$ the same as before. Also in this case, forces and couples are obtained by superposition principle and are the sum of three terms. The first one, $\mathbf{k}_b^e \mathbf{u}^e$, corresponding to the classical elastic beam, the second and the third, $\mathbf{k}_{wf}^e \boldsymbol{\Delta}\,\mathbf{u}^{e,a}$ and $\mathbf{k}_{wf}^e \boldsymbol{\Delta}\,\mathbf{u}^{e,b}$, related to the Winkler foundation.

3.1.3. Energetics of the discrete system

The elastic energy of the unit cell, W, derives from that of the three beams it consists of and it depends on the displacements and rotations of the external nodes.

First of all, it is not difficult to see that the first node of each beam coincides with the central node (0). Therefore, denoted by $\mathbf{u}_0$ the displacements of the node (0) and by $\boldsymbol{\Delta}\,\mathbf{u}_0^a$, $\boldsymbol{\Delta}\,\mathbf{u}_0^b$ the elongation of the springs in (0), follows $\mathbf{u}_i = \mathbf{u}_0$, $\boldsymbol{\Delta}\,\mathbf{u}_i^a = \boldsymbol{\Delta}\,\mathbf{u}_0^a$ and $\boldsymbol{\Delta}\,\mathbf{u}_i^b = \boldsymbol{\Delta}\,\mathbf{u}_0^b$. Moreover, (24) takes the form

$$\mathbf{f}^e = \begin{bmatrix} \mathbf{f}_0 \\ \mathbf{f}_j \end{bmatrix} = \begin{bmatrix} \mathbf{k}_{b,01}\,\mathbf{u}_j + \mathbf{k}_{b,00}\,\mathbf{u}_0 \\ \mathbf{k}_{b,11}\,\mathbf{u}_j + \mathbf{k}_{b,10}\,\mathbf{u}_0 \end{bmatrix}$$
$$+ \begin{bmatrix} \mathbf{k}_{wf,01}\,\boldsymbol{\Delta}\,\mathbf{u}_j^a + \mathbf{k}_{wf,00}\,\boldsymbol{\Delta}\,\mathbf{u}_0^a \\ \mathbf{k}_{wf,11}\,\boldsymbol{\Delta}\,\mathbf{u}_j^a + \mathbf{k}_{wf,10}\,\boldsymbol{\Delta}\,\mathbf{u}_0^a \end{bmatrix}$$
$$+ \begin{bmatrix} \mathbf{k}_{wf,01}\,\boldsymbol{\Delta}\,\mathbf{u}_j^b + \mathbf{k}_{wf,00}\,\boldsymbol{\Delta}\,\mathbf{u}_0^b \\ \mathbf{k}_{wf,11}\,\boldsymbol{\Delta}\,\mathbf{u}_j^b + \mathbf{k}_{wf,10}\,\boldsymbol{\Delta}\,\mathbf{u}_0^b \end{bmatrix}, \tag{25}$$
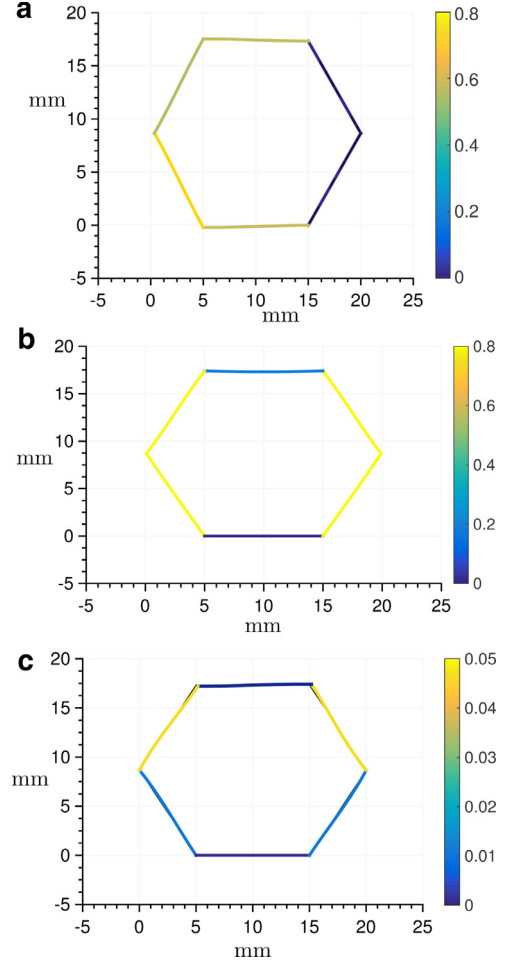
Fig. 7. The hybrid system continuum-springs: filling material as a Winkler foundation. Longitudinal stress (GPa) along the beams with $K_w = 10^{-1}$ GPa in the case of (a) Uniaxial compression in the $\mathbf{e}_1$ direction and applied forces of $10^{-3} N$, (b) Uniaxial compression in the $\mathbf{e}_2$ direction and applied forces of $10^{-3} N$, (c) Shear forces of 10^{-5} N.

where $\mathbf{f}_0$ and $\mathbf{f}_j$ are, respectively, the forces and moments of the central and external nodes $j = 1, 2, 3$. A mere partition of $\mathbf{k}_b^e$ and $\mathbf{k}_{wf}^e$ leads to the matrices

$$\mathbf{k}_{b,11} = \begin{bmatrix} C_\ell/\ell & 0 & 0 \\ 0 & 12D_\ell/\ell^3 & -6D_\ell/\ell^2 \\ 0 & -6D_\ell/\ell^2 & 4D_\ell/\ell \end{bmatrix},$$

$$\mathbf{k}_{wf,11} = \begin{bmatrix} 0 & 0 & 0 \\ 0 & 13K_w/35 & -11K_w\ell/210 \\ 0 & -11K_w\ell/210 & K_w\ell^2/105 \end{bmatrix},$$

$$\mathbf{k}_{b,10} = \begin{bmatrix} -C_\ell/\ell & 0 & 0 \\ 0 & -12D_\ell/\ell^3 & -6D_\ell/\ell^2 \\ 0 & 6D_\ell/\ell^2 & 2D_\ell/\ell \end{bmatrix},$$

$$\mathbf{k}_{wf,10} = \begin{bmatrix} 0 & 0 & 0 \\ 0 & 9K_w/70 & 13K_w\ell/420 \\ 0 & -13K_w\ell/420 & -K_w\ell^2/140 \end{bmatrix},$$

$$\mathbf{k}_{b,01} = \begin{bmatrix} -C_\ell/\ell & 0 & 0 \\ 0 & -12D_\ell/\ell^3 & 6D_\ell/\ell^2 \\ 0 & -6D_\ell/\ell^2 & 2D_\ell/\ell \end{bmatrix},$$
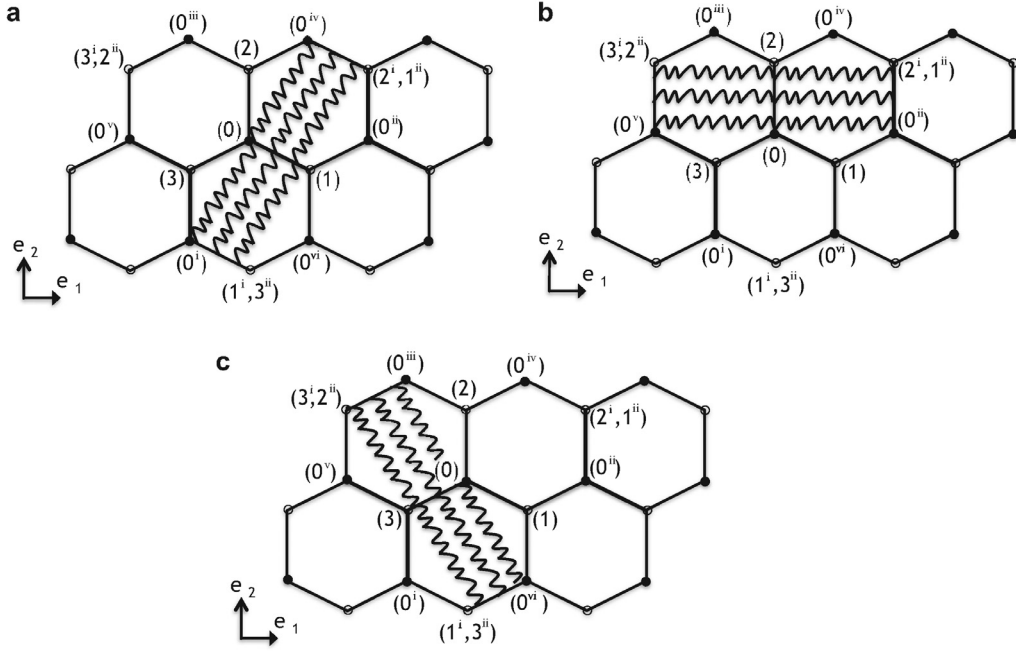
Fig. 8. The triplet of elastic beams with focus on springs. (a) Beam (0)-(1), (b) Beam (0)-(2), (c) Beam (0)-(3).
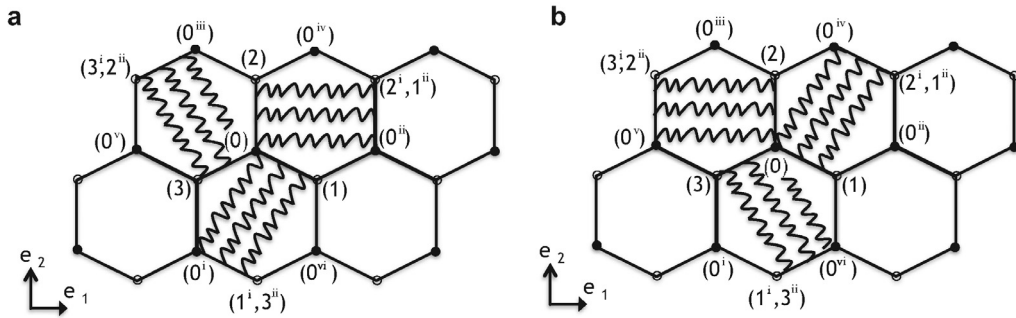

Fig. 9. The two sets of springs connecting the triplet of elastic beams. (a) Springs a, (b) Springs b.

$$\mathbf{k}_{wf,01} = \begin{bmatrix} 0 & 0 & 0 \\ 0 & 9K_w/70 & -13K_w\ell/420 \\ 0 & 13K_w\ell/420 & -K_w\ell^2/140 \end{bmatrix},$$

$$\mathbf{k}_{b,00} = \begin{bmatrix} C_\ell/\mathit{ell} & 0 & 0 \\ 0 & 2D_\ell/\ell^3 & 6D_\ell/\ell^2 \\ 0 & 6D_\ell/\ell^2 & 4D_\ell/\ell \end{bmatrix},$$

$$\mathbf{k}_{wf,00} = \begin{bmatrix} 0 & 0 & 0 \\ 0 & 13K_w/35 & 11K_w\ell/210 \\ 0 & 11K_w\ell/210 & K_w\ell^2/105 \end{bmatrix}. \quad (26)$$

Then, expressing (24) in the global reference (see Appendix B), adding up forces at the central node (0) and condensing the corresponding degrees of freedom to take account of the forces balance in (0), as in (Davini and Ongaro, 2011), leads to

$$W = W(\mathbf{u}_1, \mathbf{u}_2, \mathbf{u}_3, \boldsymbol{\Delta}\mathbf{u}_1^a, \boldsymbol{\Delta}\mathbf{u}_2^a, \boldsymbol{\Delta}\mathbf{u}_3^a, \boldsymbol{\Delta}\mathbf{u}_1^b, \boldsymbol{\Delta}\mathbf{u}_2^b, \boldsymbol{\Delta}\mathbf{u}_3^b).$$
$$(27)$$

3.2. The continuum model

3.2.1. Energy

The assumption that in the limit $\ell \to 0$ there exist the *continuous displacement and microrotation fields*, $\hat{\mathbf{u}}(\cdot)$ and $\hat{\varphi}(\cdot)$, and that the discrete variables $(\mathbf{u}_j, \varphi_j)$ previously introduced to represent the degrees of freedom (displacements and rotations) of the external nodes of the unit cell can be expressed by

$$\mathbf{u}_j = \hat{\mathbf{u}}_0 + \nabla\hat{\mathbf{u}}\,\mathbf{b}_j, \quad \varphi_j = \hat{\varphi}_0 + \nabla\hat{\varphi}\,\mathbf{b}_j, \quad j = 1, 2, 3, \quad (28)$$

provides the continuum description of the discrete structure. The terms $\mathbf{b}_j$ in (28) are the vectors formerly defined while $\hat{\mathbf{u}}_0$ and $\hat{\varphi}_0$ are the values of $\hat{\mathbf{u}}(\cdot)$ and $\hat{\varphi}(\cdot)$ at the central point of the cell in the continuum description. Substituting (28) into (7) gives the strain energy of the unit cell as a function of the fields $\hat{\mathbf{u}}$ and $\hat{\varphi}$. Note that the continuous displacement $\hat{\mathbf{u}}(\cdot)$ is referred to the global reference and $\hat{\mathbf{u}}(\cdot)$ stands for $\hat{\mathbf{U}}(\cdot)$. Also in (28), $\mathbf{u}_j$, $\hat{\mathbf{u}}_0$ and $\nabla\hat{\mathbf{u}}$ stands for $\mathbf{U}_j$, $\hat{\mathbf{U}}_0$ and $\nabla\hat{\mathbf{U}}$. The use of lowercase letters simplifies

the notation and, in what follows, $\hat{\mathbf{u}}$ and $\hat{\varphi}$ stand for $\hat{\mathbf{u}}_0$ and $\hat{\varphi}_0$.

Dividing the expression that turns out from the calculation by the area of the unit cell, A_0, gives the strain energy density in the continuum approximation w. The following relation summarize the adopted procedure:

$$\frac{W(\mathbf{U}, \varphi)}{A_0} \cong \frac{W(\hat{\mathbf{u}}, \hat{\varphi})}{A_0} = w. \tag{29}$$

In particular, the resulting energy density

$$w = w\big(\varepsilon_{\alpha\beta}, (\omega - \hat{\varphi}), \hat{\varphi}_{,\alpha}\big) \tag{30}$$

is a function of the infinitesimal strains $\varepsilon_{\alpha\beta} = \frac{1}{2}(\hat{u}_{\alpha,\beta} + \hat{u}_{\beta,\alpha})$ and the infinitesimal rotation $\omega = \frac{1}{2}(\hat{u}_{1,2} - \hat{u}_{2,1})$ that represent, respectively, the symmetric and skew-symmetric part of $\nabla\hat{\mathbf{u}}$ as in the classical continuum mechanics. $\hat{\varphi}_{,\alpha}$ are the microrotation gradients. Its explicit expression is

In particular, it emerges that $\boldsymbol{\sigma}$ is a non-symmetric tensor and its components are

$$\sigma_{\gamma\delta} = \frac{\partial w}{\partial \hat{u}_{\gamma,\delta}} = \frac{\partial w}{\partial \varepsilon_{\alpha\beta}} \frac{\partial \varepsilon_{\alpha\beta}}{\partial \hat{u}_{\gamma,\delta}} + \frac{\partial w}{\partial \omega} \frac{\partial \omega}{\partial \hat{u}_{\gamma,\delta}}, \quad \alpha, \beta, \gamma, \delta = 1, 2, \tag{35}$$

where w is the strain energy density defined in (33). By observing that

$$\frac{\partial w}{\partial \varepsilon_{\alpha\beta}} \frac{\partial \varepsilon_{\alpha\beta}}{\partial \hat{u}_{\gamma,\delta}} = \frac{1}{2}\left(\frac{\partial w}{\partial \varepsilon_{\gamma\delta}} + \frac{\partial w}{\partial \varepsilon_{\delta\gamma}}\right) = \frac{\partial w}{\partial \varepsilon_{\gamma\delta}} \equiv \sigma_{\gamma\delta}^{sym},$$

$$\frac{\partial w}{\partial \omega} \frac{\partial \omega}{\partial \hat{u}_{\gamma,\delta}} = \frac{1}{2}\frac{\partial w}{\partial \omega}\left(\delta_{1\gamma}\,\delta_{2\delta} - \delta_{2\gamma}\,\delta_{1\delta}\right)$$

$$= \frac{1}{2}\frac{\partial w}{\partial \omega}\,e_{\gamma\delta} \equiv \sigma_{\gamma\delta}^{skw}, \tag{36}$$

with $e_{\gamma\delta}$ the alternating symbol ($e_{11} = e_{22} = 0, e_{12} = -e_{21} = 1$) and δ_{ij} the Kronecker delta ($\delta_{ij} = 1$ if $i = j$, $\delta_{ij} = 0$ if $i \neq j$), follows

$$w = \frac{\big(\varepsilon_{11}^2 + \varepsilon_{22}^2\big)(C_\ell^2\ell^4 + 36D_\ell C_\ell\ell^2) + 2\varepsilon_{11}\varepsilon_{22}(C_\ell^2\ell^4 - 12D_\ell C_\ell\ell^2) + 96D_\ell C_\ell\ell^2\varepsilon_{12}^2 + 48D_\ell C_\ell\ell^3\,\varepsilon_{12}\hat{\varphi}_{,2}}{4\sqrt{3}\ell^3(12D_\ell + C_\ell\ell^2)}$$

$$+ \frac{24D_\ell C_\ell\ell^3(\varepsilon_{22} - \varepsilon_{11})\hat{\varphi}_{,1} + 8D_\ell\ell^2(3D_\ell + C_\ell\ell^2)\big(\hat{\varphi}_{,1}^2 + \hat{\varphi}_{,2}^2\big) + 12D_\ell(12D_\ell + C_\ell\ell^2)\big(\omega - \hat{\varphi}\big)^2}{4\sqrt{3}\ell^3(12D_\ell + C_\ell\ell^2)}$$

$$+ \frac{K_w\big(813\big(\varepsilon_{11}^2 + \varepsilon_{22}^2\big) + 1224\varepsilon_{12}^2 + 402\varepsilon_{11}\varepsilon_{22}\big)}{2496\sqrt{3}} + \frac{K_w\ell\big(-12\varepsilon_{12}\hat{\varphi}_{,2} + \ell(\hat{\varphi}_{,1}^2 + \hat{\varphi}_{,2}^2) + 6\hat{\varphi}_{,1}(\varepsilon_{11} - \varepsilon_{22})\big)}{96\sqrt{3}}. \tag{31}$$

After rewriting (31) in terms of $c \equiv C_\ell/\ell = \frac{E_s(h/\ell)}{1 - \nu_s^2}$ and $d \equiv D_\ell/\ell^3 = \frac{E_s(h/\ell)^3}{12(1 - \nu_s^2)}$, it emerges that in the energy obtained from the calculation the coefficients scale with different order in ℓ, as in (Davini and Ongaro, 2011):

$$\sigma_{\gamma\delta} = \sigma_{\gamma\delta}^{sym} + \sigma_{\gamma\delta}^{skw}, \quad \gamma, \delta = 1, 2, \tag{37}$$

that is

$$\sigma_{1\delta} = \sigma_{1\delta}^{sym} + \frac{1}{2}\left(\frac{\partial w}{\partial \omega}\right)e_{1\delta}, \quad \sigma_{2\delta} = \sigma_{2\delta}^{sym} + \frac{1}{2}\left(\frac{\partial w}{\partial \omega}\right)e_{2\delta}, \quad \delta = 1, 2. \tag{38}$$

$$w = \frac{\big(\varepsilon_{11}^2 + \varepsilon_{22}^2\big)(c^2 + 36\,cd) + 2\varepsilon_{11}\varepsilon_{22}(c^2 - 12\,cd) + 96\,cd\,\varepsilon_{12}^2 + 48\,cd\,\varepsilon_{12}\,\ell\hat{\varphi}_{,2}}{4\sqrt{3}(12\,d + c)}$$

$$+ \frac{24\,cd(\varepsilon_{22} - \varepsilon_{11})\,\ell\hat{\varphi}_{,1} + 8\,d(3d + c)\,\ell^2\big(\hat{\varphi}_{,1}^2 + \hat{\varphi}_{,2}^2\big) + 12\,d(12d + c)\big(\omega - \hat{\varphi}\big)^2}{4\sqrt{3}(12d + c)}$$

$$+ \frac{K_w\big(813\big(\varepsilon_{11}^2 + \varepsilon_{22}^2\big) + 1224\varepsilon_{12}^2 + 402\varepsilon_{11}\varepsilon_{22}\big)}{2496\sqrt{3}} + \frac{K_w\big(-12\varepsilon_{12}\,\ell\hat{\varphi}_{,2} + \ell^2(\hat{\varphi}_{,1}^2 + \hat{\varphi}_{,2}^2) + 6\,\ell\hat{\varphi}_{,1}(\varepsilon_{11} - \varepsilon_{22})\big)}{96\sqrt{3}}. \tag{32}$$

Specifically, the coefficients in (32) are independent of ℓ, with the exception of the microrotation gradients that scale with first order in ℓ. Consequently, in the limit $\ell \to 0$ the contribution of the microrotation gradients is missing and the equivalent continuum is non-polar, differently from (Chen et al., 1998). Accordingly, the strain energy density in the continuum approximation takes the form:

Also,

$$\frac{\partial w}{\partial \omega} = \frac{\partial w}{\partial(\omega - \hat{\varphi})} \frac{\partial(\omega - \hat{\varphi})}{\partial \omega} = \frac{\partial w}{\partial(\omega - \hat{\varphi})}. \tag{39}$$

Accordingly,

$$w = \frac{\big(\varepsilon_{11}^2 + \varepsilon_{22}^2\big)(C_\ell^2\ell^4 + 36D_\ell C_\ell\ell^2) + 2\varepsilon_{11}\varepsilon_{22}(C_\ell^2\ell^4 - 12D_\ell C_\ell\ell^2) + 96D_\ell C_\ell\ell^2\varepsilon_{12}}{4\sqrt{3}\ell^3(12D_\ell + C_\ell\ell^2)}$$

$$+ \frac{3D_\ell\big(\omega - \hat{\varphi}\big)^2}{\sqrt{3}\ell^3} + \frac{K_w\big(271\big(\varepsilon_{11}^2 + \varepsilon_{22}^2\big) + 408\varepsilon_{12}^2 + 134\varepsilon_{11}\varepsilon_{22}\big)}{832\sqrt{3}}. \tag{33}$$

3.2.2. Constitutive equations

The constitutive equations

$$\sigma = \frac{1}{A_0} \frac{\partial W}{\partial \nabla\hat{\mathbf{u}}}, \tag{34}$$

with $\boldsymbol{\sigma}$ the Cauchy-type stress tensor, ensue from (33).

$$\sigma_{11} = \sigma_{11}^{sym} = \frac{(C_\ell^2\ell^2 + 36D_\ell C_\ell)\varepsilon_{11} + (C_\ell^2\ell^2 - 12D_\ell C_\ell)\varepsilon_{22}}{2\sqrt{3}\,\ell(12D_\ell + C_\ell\ell^2)}$$

$$+ \frac{K_w(271\varepsilon_{11} + 67\varepsilon_{22})}{416\sqrt{3}},$$

$$\sigma_{22} = \sigma_{22}^{sym} = \frac{(C_\ell^2\ell^2 + 36D_\ell C_\ell)\varepsilon_{22} + (C_\ell^2\ell^2 - 12D_\ell C_\ell)\varepsilon_{11}}{2\sqrt{3}\,\ell(12D_\ell + C_\ell\ell^2)}$$

$$+ \frac{K_w(271\varepsilon_{22} + 67\varepsilon_{11})}{416\sqrt{3}},$$

$$\sigma_{12}^{sym} = \sigma_{21}^{sym} = \frac{48D_\ell C_\ell \varepsilon_{12}}{2\sqrt{3}\,\ell(12D_\ell + C_\ell\ell^2)} + \frac{51K_w\,\varepsilon_{12}}{52\sqrt{3}},$$

$$\sigma_{12}^{skw} = -\sigma_{21}^{skw} = \frac{\sqrt{3}\,D_\ell\big(\omega - \hat{\varphi}\big)}{\ell^3},$$

$$\sigma_{12} = \sigma_{12}^{sym} + \sigma_{12}^{skw}, \quad \sigma_{21} = \sigma_{21}^{sym} + \sigma_{21}^{skw}, \tag{40}$$

been $\sigma_{\gamma\delta}^{sym}$ and $\sigma_{\gamma\delta}^{skw}$, in turn, the symmetric and skew-symmetric parts of $\boldsymbol{\sigma}$.

3.2.3. Elastic constants

The constitutive equations derived so far enables us to get the effective elastic constants in the continuum approximation by adopting the following approach.

First of all, let us consider a stress state where $\sigma_{11} \neq 0$, $\sigma_{22} = \sigma_{12} = \sigma_{21} = 0$. In view of (40) and from Hooke's law $\sigma_{11}^{sym} = E_1^* \varepsilon_{11}$, the Young's modulus in the $\mathbf{e}_1$ direction is:

$$E_1^* = \frac{(13K_w(1 - \nu_s^2) + 16\lambda E_s)(51(1 + \lambda^2)K_w(1 - \nu_s^2) + 208\lambda^3 E_s)}{4\sqrt{3}(1 - \nu_s^2)(271(1 + \lambda^2)K_w(1 - \nu_s^2) + 208(\lambda + 3\lambda^3)E_s)}, \tag{41}$$

with E_s, ν_s and $\lambda = (h/\ell)$ respectively, the Young's modulus and the Poisson's ratio of the cell walls material, and the ratio between the thickness and the length of the cell arms.

The related Poisson's ratio $\nu_{12}^* = -\varepsilon_{22}/\varepsilon_{11}$ takes the form:

$$\nu_{12}^* = \frac{67(1 + \lambda^2)K_w(1 - \nu_s^2) - 208\lambda(\lambda^2 - 1)E_s}{271(1 + \lambda^2)K_w(1 - \nu_s^2) + 208\lambda(1 + 3\lambda^2)E_s}. \tag{42}$$

A stress state defined as $\sigma_{22} \neq 0$, $\sigma_{11} = \sigma_{12} = \sigma_{21} = 0$ leads, with analogous calculations, to the Young's modulus in the $\mathbf{e}_2$ direction and to the related Poisson's ratio $\nu_{21}^* = -\varepsilon_{11}/\varepsilon_{22}$. In particular, it emerges that $E_1^* = E_2^* \equiv E^*$ and $\nu_{12}^* = \nu_{21}^* \equiv \nu^*$, where E^* and ν^* stands for the Young's modulus, the first, and the Poisson's ratio, the second, of the approximated continuum.

Moreover, the stress state $\sigma_{12}^{sym} \neq 0$, $\sigma_{11} = \sigma_{22} = 0$ yields the tangential elastic modulus $G^* = \sigma_{12}^{sym}/2\,\varepsilon_{12}$:

$$G^* = \frac{51(1 + \lambda^2)K_w(1 - \nu_s^2) + 208\lambda^3 E_s}{208\sqrt{3}(1 + \lambda^2)(1 - \nu_s^2)}. \tag{43}$$

Finally, the above moduli E^*, ν^*, G^* satisfy the classical relation $G^* = \dfrac{E^*}{2(1 + \nu^*)}$, typical of the isotropic materials.

4. Discussion

4.1. Comparison between the analytical and numerical homogenization

The compact expression of the constitutive equations derived so far is

$$\begin{bmatrix} \sigma_{11}^{sym} \\ \sigma_{22}^{sym} \\ \sigma_{12}^{sym} \end{bmatrix} = \begin{bmatrix} C_{11} & C_{12} & C_{13} \\ C_{21} & C_{22} & C_{23} \\ C_{31} & C_{32} & C_{33} \end{bmatrix} \begin{bmatrix} \varepsilon_{11} \\ \varepsilon_{22} \\ \varepsilon_{12} \end{bmatrix} \tag{44}$$

or, in terms of strain,

$$\begin{bmatrix} \varepsilon_{11} \\ \varepsilon_{22} \\ \varepsilon_{12} \end{bmatrix} = \begin{bmatrix} C_{11}^* & C_{12}^* & C_{13}^* \\ C_{21}^* & C_{22}^* & C_{23}^* \\ C_{31}^* & C_{32}^* & C_{33}^* \end{bmatrix} \begin{bmatrix} \sigma_{11}^{sym} \\ \sigma_{22}^{sym} \\ \sigma_{12}^{sym} \end{bmatrix} \tag{45}$$

with

$$C_{11}^* = C_{22}^* = \frac{C_{22}C_{33}}{C_{22}^2 C_{33} - C_{12}^2 C_{33}}$$
$$= \frac{2\sqrt{3}(1 - \nu_s^2)(271(1 + \lambda^2)K_w(1 - \nu_s^2) + 104(\lambda + 3\lambda^3)E_s)}{(13K_w(1 - \nu_s^2) + 8\lambda E_s)(51(1 + \lambda^2)K_w(1 - \nu_s^2) + 104\lambda^3 E_s)},$$

$$C_{12}^* = C_{21}^* = -\frac{C_{12}C_{33}}{C_{22}^2 C_{33} - C_{12}^2 C_{33}}$$
$$= -\frac{4\sqrt{3}(1 - \nu_s^2)(271(1 + \lambda^2)K_w(1 - \nu_s^2) - 208(\lambda^3 - \lambda)E_s)}{(13K_w(1 - \nu_s^2) + 16\lambda E_s)(51(1 + \lambda^2)K_w(1 - \nu_s^2) + 208\lambda^3 E_s)},$$

$$C_{33}^* = \frac{C_{22}^2 - C_{12}^2}{C_{22}^2 C_{33} - C_{12}^2 C_{33}}$$
$$= \frac{52\sqrt{3}(1 - \nu_s^2)(1 + \lambda^2)}{51K_w(1 - \nu_s^2)(1 + \lambda^2) + 104E_s\lambda^3},$$

$$C_{13}^* = C_{23}^* = C_{31}^* = C_{32}^* = 0. \tag{46}$$

The constants C_{ij}, derived in Section 3, are listed as

$$C_{11} = C_{22} = \frac{C_\ell^2 \ell^2 + 36D_\ell C_\ell}{2\sqrt{3}\,\ell(12D_\ell + C_\ell\ell^2)} + \frac{271\,K_w}{416\sqrt{3}},$$

$$C_{12} = C_{21} = -\frac{C_\ell^2 \ell^2 - 12D_\ell C_\ell}{2\sqrt{3}\,\ell(12D_\ell + C_\ell\ell^2)} + \frac{67\,K_w}{416\sqrt{3}},$$

$$C_{33} = \frac{48D_\ell C_\ell}{2\sqrt{3}\,\ell(12D_\ell + C_\ell\ell^2)} + \frac{51\,K_w}{52\sqrt{3}},$$

$$C_{13} = C_{23} = C_{31} = C_{32} = 0. \tag{47}$$

Finite element simulations on a computational model of the microstructure assess the analytical approach. In particular, the Euler-Bernoulli beam on Winkler foundation elements represent the composite hexagonal microstructure. The cell wall material, isotropic linear elastic for assumption, has Young's modulus E_s and Poisson's ratio ν_s, respectively, of 79 GPa and 0.35, thickness $h = 0.1\ell$ and $K_w = 0.0001E_s$.

The displacements and the derived quantities at every point within the beam are obtained by interpolation, using the same shape functions:

$$\mathbf{u}(\xi) = \mathbf{N}(\xi)\,\mathbf{u}^e, \tag{48}$$

been ξ a parametric coordinate along the length of the beam $(-1 \leq \xi \leq 1)$, $\mathbf{u}(\xi) = [u(\xi)\,v(\xi)]$ and $\mathbf{u}^e = [u_i^e\,v_i^e\,\varphi_i^e\,u_j^e\,v_j^e\,\varphi_j^e]$, respectively, the displacements at any value of ξ and the local displacements of the extreme nodes of the beam,

$$\mathbf{N}(\xi) = \begin{bmatrix} N_1 & 0 & 0 & N_2 & 0 & 0 \\ 0 & N_3 & N_4 & 0 & N_5 & N_6 \end{bmatrix} \tag{49}$$

the shape functions matrix. In particular,

$$N_1 = \frac{1 - \xi}{2}, \quad N_2 = \frac{1 + \xi}{2},$$

$$N_3 = \frac{1 - \xi(3 - \xi^2)/2}{2},$$

$$N_4 = \frac{\ell(1-\xi^2)(1-\xi)}{8}, \quad N_5 = \frac{1+\xi(3-\xi^2)/2}{2},$$
$$N_6 = -\frac{\ell(1-\xi^2)(1+\xi)}{8}. \tag{50}$$

This study involves a 75×50 mm rectangular domain discretized in an increasing number of hexagonal cells of gradually smaller length ℓ. The load conditions considered are the uniaxial compression and uniaxial traction in the directions $\mathbf{e}_1$ and $\mathbf{e}_2$, and pure shear. Also, forces acting at the unconstrained boundary nodes of the domain simulate the basic loading states. The corresponding effective stiffness components are calculated as the ratio between the average volume strain,

$$\overline{\varepsilon}_{ij} = \frac{1}{V} \int_V \varepsilon_{ij} \, dV, \quad i,j = 1,2, \tag{51}$$

and the applied stress. Specifically, when the forces act horizontally, (45) leads to

$$\overline{\varepsilon}^{(1)} = \begin{bmatrix} \overline{\varepsilon}_{11}^{(1)} \\ \overline{\varepsilon}_{22}^{(1)} \\ \overline{\varepsilon}_{12}^{(1)} \end{bmatrix} = \begin{bmatrix} C_{11}^* & C_{12}^* & C_{13}^* \\ C_{21}^* & C_{22}^* & C_{23}^* \\ C_{31}^* & C_{32}^* & C_{33}^* \end{bmatrix} \begin{bmatrix} \sigma_{11} \\ 0 \\ 0 \end{bmatrix} = \begin{bmatrix} C_{11}^*\sigma_{11} \\ C_{21}^*\sigma_{11} \\ C_{31}^*\sigma_{11} \end{bmatrix}, \tag{52}$$

been σ_{11} the applied stress and $\overline{\varepsilon}^{(1)}$ the corresponding strain vector. Consequently,

$$C_{11}^* = \frac{\overline{\varepsilon}_{11}^{(1)}}{\sigma_{11}}, \quad C_{21}^* = \frac{\overline{\varepsilon}_{22}^{(1)}}{\sigma_{11}}, \quad C_{31}^* = \frac{\overline{\varepsilon}_{12}^{(1)}}{\sigma_{11}}, \tag{53}$$

where

$$\overline{\varepsilon}_{ij}^{(1)} = \frac{1}{V} \int_V \varepsilon_{ij}^{(1)} \, dV, \quad i,j = 1,2, \tag{54}$$

and V is the volume of the domain. Because of the present analysis involves a domain with unitary width, composed by a sequence of discrete beams having the same length ℓ and the same thickness h, (54) turns out to be

$$\overline{\varepsilon}_{ij}^{(1)} = \frac{\sum_{m=1}^{n_b} \left(\int \varepsilon_{ij}^{(1)}(s) \, ds \right)_m}{\sum_{m=1}^{n_b} \left(\int ds \right)_m} = \frac{\sum_{m=1}^{n_b} \left(\int \varepsilon_{ij}^{(1)}(s) \, ds \right)_m}{n_b \, \ell},$$
$$i,j = 1,2, \tag{55}$$

with s a parametric coordinate along the length of the beam ($0 \leq s \leq \ell$), Ω the area of the domain and n_b the number of the beams.

Remembering that

$$\varepsilon_{ij}(s) = \frac{1}{2} \left(\frac{\partial u_i(s)}{\partial x_j} + \frac{\partial u_j(s)}{\partial x_i} \right) \tag{56}$$

and that

$$\frac{\partial u_i(s)}{\partial x_j} = \frac{\partial u_i(s)}{\partial s} \frac{\partial s}{\partial x_j}, \quad \frac{\partial u_j(s)}{\partial x_i} = \frac{\partial u_j(s)}{\partial s} \frac{\partial s}{\partial x_i}, \quad i,j = 1,2, \tag{57}$$

gives

$$\overline{\varepsilon}_{ij}^{(1)} = \frac{\sum_{m=1}^{n_b} \frac{1}{2} \left((u_i(\ell) - u_i(0)) \frac{\partial s}{\partial x_j} + (u_j(\ell) - u_j(0)) \frac{\partial s}{\partial x_i} \right)_m}{n_b \, \ell}. \tag{58}$$

In Cartesian coordinates, $s = (\cos\theta, \sin\theta)$, been θ the angle of inclination of the beam with respect to the x-axis. Accordingly,

$$\frac{\partial s}{\partial x_j} = \cos\theta \, \delta_{1j} + \sin\theta \, \delta_{2j}, \quad \frac{\partial s}{\partial x_i} = \cos\theta \, \delta_{1i} + \sin\theta \, \delta_{2i},$$
$$i,j = 1,2, \tag{59}$$

with δ_{ij} the Kroneker delta. The classical continuum mechanics provides the Young's modulus, E_1^*, and the related Poisson's ratio v_{12}^*:

$$E_1^* = \frac{\sigma_{11}}{\overline{\varepsilon}_{11}^{(1)}}, \quad v_{12}^* = -\frac{\overline{\varepsilon}_{22}^{(1)}}{\overline{\varepsilon}_{11}^{(1)}}. \tag{60}$$

With analogous calculations, forces acting vertically provide

$$\overline{\varepsilon}^{(2)} = \begin{bmatrix} \overline{\varepsilon}_{11}^{(2)} \\ \overline{\varepsilon}_{22}^{(2)} \\ \overline{\varepsilon}_{12}^{(2)} \end{bmatrix} = \begin{bmatrix} C_{11}^* & C_{12}^* & C_{13}^* \\ C_{21}^* & C_{22}^* & C_{23}^* \\ C_{31}^* & C_{32}^* & C_{33}^* \end{bmatrix} \begin{bmatrix} 0 \\ \sigma_{22} \\ 0 \end{bmatrix} = \begin{bmatrix} C_{12}^*\sigma_{22} \\ C_{22}^*\sigma_{22} \\ C_{32}^*\sigma_{22} \end{bmatrix} \tag{61}$$

and

$$C_{12}^* = \frac{\overline{\varepsilon}_{11}^{(2)}}{\sigma_{22}}, \quad C_{22}^* = \frac{\overline{\varepsilon}_{22}^{(2)}}{\sigma_{22}}, \quad C_{32}^* = \frac{\overline{\varepsilon}_{12}^{(2)}}{\sigma_{22}}. \tag{62}$$

As before, σ_{22} is the applied stress, $\overline{\varepsilon}^{(2)}$ the corresponding strain vector and $\overline{\varepsilon}_{ij}^{(2)}$ the average volume strain defined in (58). Regarding the elastic moduli,

$$E_2^* = \frac{\sigma_{22}}{\overline{\varepsilon}_{22}^{(2)}}, \quad v_{21}^* = -\frac{\overline{\varepsilon}_{11}^{(2)}}{\overline{\varepsilon}_{22}^{(2)}}. \tag{63}$$

Finally, in the case of in-plane shear

$$\overline{\varepsilon}^{(3)} = \begin{bmatrix} \overline{\varepsilon}_{11}^{(3)} \\ \overline{\varepsilon}_{22}^{(3)} \\ \overline{\varepsilon}_{12}^{(3)} \end{bmatrix} = \begin{bmatrix} C_{11}^* & C_{12}^* & C_{13}^* \\ C_{21}^* & C_{22}^* & C_{23}^* \\ C_{31}^* & C_{32}^* & C_{33}^* \end{bmatrix} \begin{bmatrix} 0 \\ 0 \\ \sigma_{12} \end{bmatrix} = \begin{bmatrix} C_{13}^*\sigma_{12} \\ C_{23}^*\sigma_{12} \\ C_{33}^*\sigma_{12} \end{bmatrix}, \tag{64}$$

that leads to

$$C_{13}^* = \frac{\overline{\varepsilon}_{11}^{(3)}}{\sigma_{12}}, \quad C_{23}^* = \frac{\overline{\varepsilon}_{22}^{(3)}}{\sigma_{12}}, \quad C_{33}^* = \frac{\overline{\varepsilon}_{12}^{(3)}}{\sigma_{12}}. \tag{65}$$

Again, σ_{12} is the applied stress, $\overline{\varepsilon}^{(3)}$ the corresponding strain vector and $\overline{\varepsilon}_{ij}^{(3)}$ the average volume strain defined in (58). The relation

$$G^* = \frac{\sigma_{12}}{2 \, \overline{\varepsilon}_{12}^{(3)}} \tag{66}$$

gives the tangential elastic modulus.

The results of our analysis are presented in Tables 1 and 2, that provide a comparison between the analytical and numerical values of the C_{ij}^* constants, Tables 1, and of the elastic moduli, Tables 2. As it can be seen, the results from the continuum formulation compare reasonably well with the numerical solutions.

Nevertheless, the difference between the analytical results and the numerical solutions slightly increases when the number of cells increases. This is not surprising, since

Table 1
Comparison between the analytical and numerical approach, C_{ij}^* constants.

No. cells	ℓ (mm)	C_{11}^*	C_{22}^*	C_{12}^*	C_{21}^*	C_{33}^*	$C_{13}^* = C_{23}^* = C_{31}^* = C_{32}^*$
10×7	5	2.4	2.8	−2.2	−2.1	10.1	0
50×35	1	2.3	2.3	−2.3	−2.3	9.7	0
100×70	0.5	2.4	2.4	−2.3	−2.3	5.9	0
200×140	0.25	2.3	2.4	−2.3	−2.3	4.3	0
250×175	0.2	2.3	2.3	−2.2	−2.2	3.9	0
400×280	0.125	2.2	2.2	−2.1	−2.1	3.9	0
500×350	0.1	2.2	2.2	−2.1	−2.1	3.9	0
Analytical results		2.5	2.5	−2.4	−2.4	4.8	0

Table 2
Comparison between the analytical and numerical approach, elastic moduli.

No. cells	ℓ (mm)	E_1^* (GPa)	E_2^* (GPa)	ν_{12}^*	ν_{21}^*	G^* (GPa)
10×7	5	0.42	0.44	0.91	0.92	0.03
50×35	1	0.43	0.43	1.00	0.99	0.05
100×70	0.5	0.42	0.42	0.96	0.95	0.08
200×140	0.25	0.43	0.42	0.96	0.95	0.11
250×175	0.2	0.43	0.44	0.95	0.96	0.13
400×280	0.125	0.44	0.45	0.95	0.96	0.13
500×350	0.1	0.44	0.44	0.95	0.95	0.13
Analytical results		0.40	0.40	0.96	0.96	0.10

the assumptions of the theoretical model inevitably introduce approximations that are as significant as the number of cells increases. That is, the condensation of the degrees of freedom of the central node, the introduction of the linear interpolants of nodal displacements and rotations in the discrete energy of the system to obtain the continuum model, the filling material represented by a Winkler foundation. In particular, condensing the degrees of freedom of the central node subordinates the freedom of the nodes of lattice L_2 to that of lattice L_1 and, in contrast to the numerical model, gives the two lattices a different role (Davini and Ongaro, 2011). Regarding the approximation introduced by the linear interpolants, one could improve the analytical predictions by the use of asymptotic expansions as (Chen et al., 1998), (Gonella and Ruzzene, 2008), (Dos Reis and Ganghoffer, 2012). Also, this could lead to a micropolar continuum as in (Chen et al., 1998) and (Dos Reis and Ganghoffer, 2012). Finally, as stated, representing the filling material by a Winkler foundation is a simplification aimed at obtaining a mathematically tractable problem. This obviously implies approximations that could be improved by modeling the filling material by a more complex model, as the Winkler–Pasternak foundation, (Limkatanyu et al., 2014), (Civalek, 2007), (Kerr, 1964).

4.2. Comparison with other works

Recent works focus on the mechanical characterization of cellular materials with an unfilled honeycomb microstructure. A comparison between the proposed results and the available analytical solutions for unfilled honeycombs verify the adopted modeling strategy. Obviously, it is necessary to neglect the presence of the filling material, represented by a Winkler foundation, and assume $k_w = 0$. So, the composite cellular material of the present approach reduces to a traditional cellular material with a honeycomb-like microstructure and the elastic moduli in

(41), (42), (43) are now listed as

$$E^* = \frac{4\sqrt{3}\lambda^3 E_s}{3\,(1 - \nu_s^2)(1 + 3\lambda^2)}, \tag{67}$$

$$\nu^* = \frac{1 - \lambda^2}{1 + 3\lambda^2}, \tag{68}$$

$$G^* = \frac{\sqrt{3}\lambda^3 E_s}{3\,(1 - \nu_s^2)(1 + \lambda^2)}. \tag{69}$$

Fig. 10 and Tables 3, based on a honeycomb made of an aluminum alloy with $E_s = 79$ GPa and $\nu_s = 0.35$, illustrate the results of the analysis. It emerges that the above expressions coincide with those in (Davini and Ongaro, 2011), where the authors deduced the constitutive model for the in-plane deformations of a honeycomb through an energy approach in conjunction with the homogenization theory. In particular, they represented the microstructure as a sequence of elastic beams and expressed the energy in the continuum form by introducing the linear interpolants of nodal displacements and rotations in the discrete energy of the system. From general theorems of Γ-convergence, the authors obtained the homogenized model that, in contrast to (Chen et al., 1998), does not develop couple stresses. Similarly to the present paper, (Davini and Ongaro, 2011) considered the equilibrium condition at the central node and condensed the corresponding degrees of freedom.

Furthermore, as Fig. 10 shows, (67) and (69) are in accordance with (Gibson and Ashby, 2001), where the equivalent elastic moduli are obtained by applying the principles of structural analysis to the representative volume element and by assuming a prevalent mode of deformation and failure.

Regarding (Gonella and Ruzzene, 2008), the authors derived the equivalent properties of the lattice by focusing on the partial differential equations associated with the corresponding homogenized model. Differently from the present
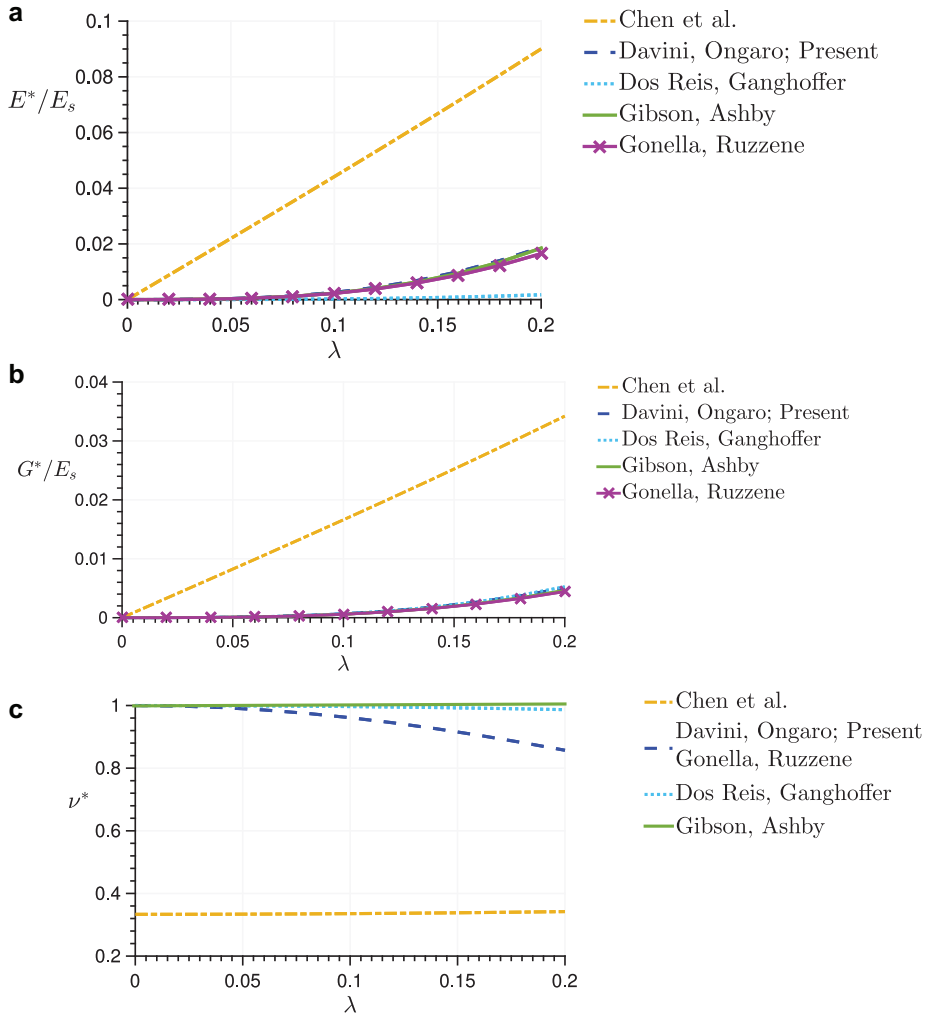
Fig. 10. Comparison between the elastic constants obtained in the present paper and those of the other authors: (a) Young's modulus, (b) Shear modulus, (c) Poisson's ratio.

Table 3

Expressions for the Young's modulus, shear modulus and Poisson's ratio derived from the models that we have compared.

Chen et al. (1998)

$$\frac{E^*_{CH}}{E_s} = \frac{2\lambda(1+\lambda^2)}{\sqrt{3}\,(1-\nu_s^2)(3+\lambda^2)} \qquad \frac{G^*_{CH}}{E_s} = \frac{\sqrt{3}\,\lambda(1+\lambda^2)}{12\,(1-\nu_s^2)} \qquad \nu^*_{CH} = \frac{1+\lambda^2}{3+\lambda^2}$$

Davini and Ongaro (2011)

$$\frac{E^*_{DO}}{E_s} = \frac{4\sqrt{3}\lambda^3}{3\,(1-\nu_s^2)(1+3\lambda^2)} \qquad \frac{G^*_{DO}}{E_s} = \frac{\sqrt{3}\,\lambda^3}{3\,(1-\nu_s^2)(1+\lambda^2)} \qquad \nu^*_{DO} = \frac{1-\lambda^2}{1+3\lambda^2}$$

Dos Reis and Ganghoffer (2012)

$$\frac{E^*_{DG}}{E_s} = \frac{\lambda+3\sqrt{\lambda^3}}{6\,(1-\nu_s^2)(1+\lambda^2)} \qquad \frac{G^*_{DG}}{E_s} = \frac{4\sqrt{3}\,\lambda^3}{(1-\nu_s^2)(12+\lambda^2)} \qquad \nu^*_{DG} = \frac{12-\lambda^2}{3(4+\lambda^2)}$$

Gibson and Ashby (2001)

$$\frac{E^*_{GA}}{E_s} = \frac{4\lambda^3}{\sqrt{3}} \qquad \frac{G^*_{GA}}{E_s} = \frac{\lambda^3}{\sqrt{3}} \qquad \nu^*_{GA} = 1$$

Gonella and Ruzzene (2008)

$$\frac{E^*_{GR}}{E_s} = \frac{4\sqrt{3}\lambda^3}{3(1+3\lambda^2)} \qquad \frac{G^*_{GR}}{E_s} = \frac{\sqrt{3}\,\lambda^3}{3\,(1+\lambda^2)} \qquad \nu^*_{GR} = \frac{1-\lambda^2}{1+3\lambda^2}$$

approach, their homogenization technique involves Taylor series expansions truncated to the second order of the displacements and rotations of the boundary nodes. Then, the assumption of no concentrated couples acting to the structure leads to a non polar continuum, slightly less stiff than that of the present paper.

An alternative technique for the analysis of periodic lattices is proposed in (Dos Reis and Ganghoffer, 2012). The authors derived the homogenized stress-strain relations under compression and shear for a 2D hexagonal lattice composed of extensional and flexural elements. In particular, the homogenization problem is performed in the framework of micropolar elasticity, where the interactions between two neighboring points involve both the Cauchy stress, as in classical mechanics, and the couple stress tensor (Eremeyev et al., 2013). Also, contrary to classical elasticity, the Cauchy tensor is not symmetrical. As Fig. 10 shows, the homogenized elastic moduli proposed in (Dos Reis and Ganghoffer, 2012) $E_{DG}^*, G_{DG}^*, \nu_{DG}$ agree with ours, E^*, G^*, ν^*, in the limit of slender beams. For instance, after writing (67) in terms of the Young's modulus in (Dos Reis and Ganghoffer, 2012), E_{DG}^*, it emerges that the two estimates differ by a quantity related to the ratio λ between the thickness and the length of the cell walls, that reduces as $\lambda \to 0$:

$$E^* = \frac{E_{DG}^* 8\lambda^2 (1+\lambda)^2}{\left(1 + 3\lambda^2\right)^2}. \tag{70}$$

In the case of (Gibson and Ashby, 2001) Young's modulus an analogous consideration applies:

$$E^* = \frac{E_{GA}^*}{\left(1 + 3\lambda^2\right)\left(1 - \nu_s^2\right)}. \tag{71}$$

An analysis of the micropolar behavior of the honeycomb microstructure is also provided in (Chen et al., 1998). The authors represented the lattice as a sequence of elastic beams and derived the continuum model by means of an asymptotic Taylor's expansion of the nodal displacements and rotations in the strain energy of the discrete structure. Differently from (Davini and Ongaro, 2011), (Gonella and Ruzzene, 2008), (Dos Reis and Ganghoffer, 2012), the approach in (Chen et al., 1998) ignores the connectivity of the beams and, in particular, the equilibrium conditions and the condensation of the degrees of freedom of the central node. They also calculated the elastic energy of the discrete structure by a superposition of the strain energies of the individual beams. This technique predicts a much stiffer behavior than the results of the other authors (Fig. 10).

As a conclusion, the present approach leads to elastic moduli that are generally in accordance with those available in the literature, with the exception of (Chen et al., 1998). As pointed out, in (Chen et al., 1998) the equilibrium conditions and the degrees of freedom of the central node are not considered. This states the major difference with respect to the present approach, in conjunction with the use of an asymptotic expansions of the displacements and rotation fields.

In addition, Table 4 summarizes the outcome of the comparison between the effective elastic constants of the present study and those of the other authors, in the case of filled honeycomb.

As it can be seen, our results are in good accordance with the predictions in (Murray et al., 2009), derived from a 2D finite element analysis of an aluminum honeycomb filled with a polymeric material. Similarly to the present approach, (Murray et al., 2009) modeled the cell walls as a Euler-Bernoulli beam elements while the infill as a plane-stress shell element.

Regarding (Burlayenko and Sadowski, 2010), the authors considered an aluminum honeycomb filled with a PVC foam and obtained the equivalent elastic moduli using a 3D finite element analysis and the strain energy homogenization technique of periodic media. Also, shell elements and brick elements represent, respectively, the cell walls and the filling material, both of them assumed isotropic. As Table 4 shows, the approach in (Burlayenko and Sadowski, 2010) leads to a slightly more stiff equivalent continuum than that of the present paper.

It should be noted that (15) provides the relation between the values of K_w and the Young's modulus of the filling material in (Murray et al., 2009), $E_{f,M}$, and in (Burlayenko and Sadowski, 2010), $E_{f,B}$, listed in Table 4. Also, for sake of clarity, in Table 4 $E_{1,M}^*, E_{2,M}^*$ and $E_{1,B}^*, E_{2,B}^*, G_B^*$ stand for the elastic constants derived in (Murray et al., 2009) and in (Burlayenko and Sadowski, 2010), respectively.

4.3. The influence of microstructure parameters in the overall properties

As it can be noted from the expressions (41)–(43), the elastic moduli in the continuum approximation are obviously related to the microstructure parameters. Such as the Young's modulus E_s and the Poisson's ratio ν_s of the cell walls material, the product $K_w = k_w \ell$ of the constant k_w of the Winkler foundation model and the length of the cell arms, the ratio $\lambda = h/\ell$ between the thickness and the length of the beams.

Figs. 11 and 12, based on an aluminum alloy with $E_s = 79$ GPa and $\nu_s = 0.35$ as before, show, in turn, the influence of K_w and of λ in the macroscopic Young's modulus E^*, shear modulus G^* and Poisson's ratio ν^*.

When λ is fixed, Fig. 11a and b suggest that both the ratio E^*/E_s and G^*/E_s increase with increasing K_w. That is to say, both the Young's modulus and shear modulus increase with increasing K_w and this is consistent with the result that one expects by increasing the stiffness of the material filling the cells (the parameter K_w). Specifically, the bigger λ, that corresponds to a beam that becomes more and more thick, the larger will be the increase of the moduli E^* and G^*. Also, an high value of λ ($\lambda = 0.2$) leads to an higher initial value of both E^* and G^* than that which occurs for a small value of λ ($\lambda = 0.02$). Regarding the Poisson's ratio ν^*, Fig. 11c shows that for fixed λ, an increase in K_w yields a decrease in the Poisson's ratio. In particular, the smaller λ, the larger will be the decrease and, as it can be seen, the smaller λ, the smaller will be the value of K_w in correspondence of which ν^* reaches its minimum value: $K_w \approx 0.025 E_s$, $K_w \approx 0.35 E_s$, $K_w \approx 0.47 E_s$, respectively for $\lambda = 0.02, 0.05, 0.1$. The initial decrease in ν^*, followed by

Table 4

Comparison between the elastic constants of the present paper and those of the other authors in the case of filled microstructure.

	(Murray et al., 2009) $E_s = 70$ GPa, $\nu_s = 0.35$, $\lambda = 0.1$		Present $E_s = 70$ GPa, $\nu_s = 0.35$, $\lambda = 0.1$	
$E_{f,M}$ (GPa)	$E_{1,M}^* = E_{2,M}^*$ (GPa)		K_w (GPa)	$E_1^* = E_2^*$ (GPa)
0.001	0.3÷0.4		0.001	0.35
0.01	0.3÷0.4		0.009	0.37
0.1	0.5		0.094	0.45
1	1.2÷1.3		0.94	1.3
	(Burlayenko and Sadowski, 2010) $E_s = 72.2$ GPa, $\nu_s = 0.34$, $\lambda = 0.0125$		Present $E_s = 72.2$ GPa, $\nu_s = 0.34$, $\lambda = 0.0125$	
$E_{f,B}$ (GPa)	$E_{1,B}^* = E_{2,B}^*$ (MPa)	G_B^* (MPa)	K_w (GPa)	$E_1^* = E_2^*$ (MPa)	G^* (MPa)
0.056	0.627	0.238	0.053	0.610	0.235
0.105	0.788	0.282	0.099	0.760	0.267
0.230	1.061	0.386	0.216	0.885	0.338

Fig. 11. The influence of K_w in the elastic constants: (a) Young's modulus, (b) Shear modulus, (c) Poisson's ratio.
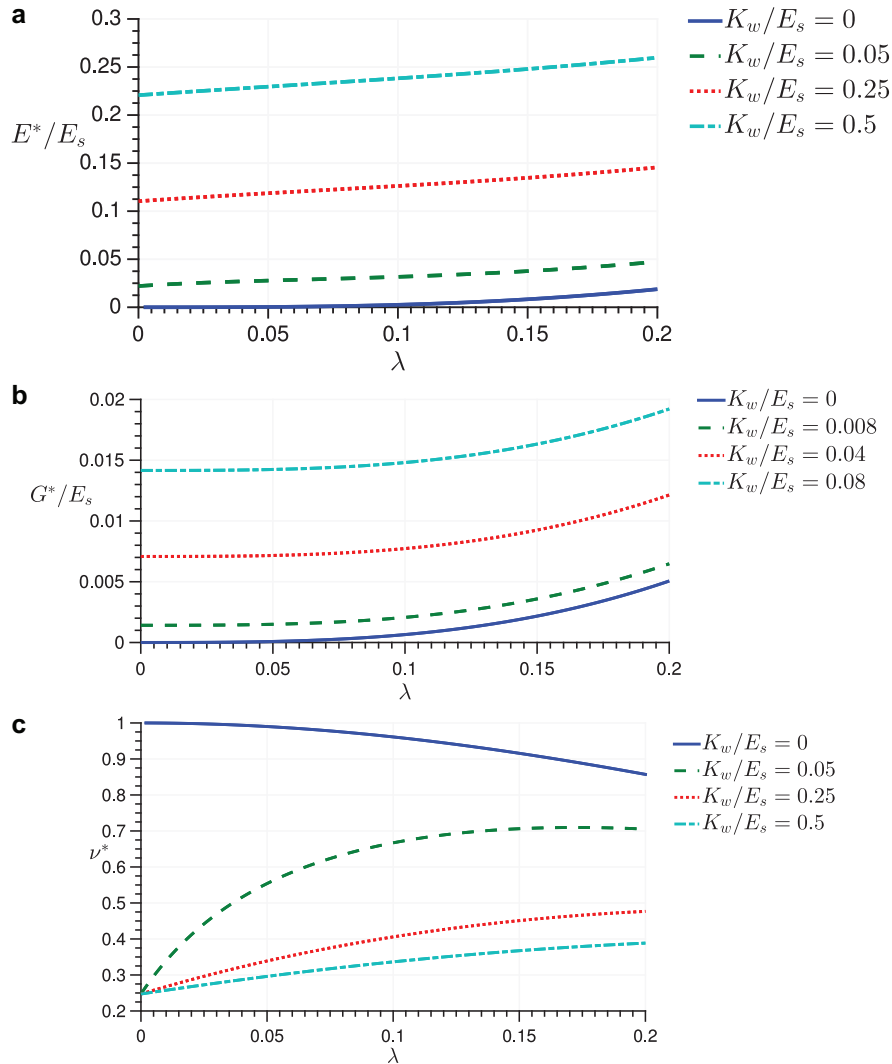
Fig. 12. The influence of λ in the elastic constants: (a) Young's modulus, (b) Shear modulus, (c) Poisson's ratio.

an almost horizontal line once K_w reaches a specific value, is larger for high values of λ. In fact, the initial slope of the curves corresponding to $\lambda = 0.1$ and $\lambda = 0.2$ is bigger than that corresponding to $\lambda = 0.02$ and $\lambda = 0.05$.

In terms of the influence of λ in the overall properties E^*, G^*, ν^*, Fig. 12a and b suggest that when K_w is fixed, the ratio E^*/E_s and G^*/E_s generally increase with increasing λ. Namely, when the beam become thicker there will be an increase in E^* and G^*. Nevertheless, to high values of K_w ($0.25\,E_s$, $0.5\,E_s$ for the Young's modulus, $0.08\,E_s$, $0.04\,E_s$ for the shear modulus) corresponds to an higher initial value of both E^* and G^* than that which occurs for small values of K_w ($0\,E_s$, $0.05\,E_s$ for the Young's modulus, $0\,E_s$, $0.008\,E_s$ for the shear modulus). Regarding the Poisson's ratio, from Fig. 12c globally emerges that when K_w is fixed, an increase in λ leads to an increase in ν^*. In particular, for high values of K_w ($0.5\,E_s$, $0.25\,E_s$) the increase is less significant than that occurring for small values of it ($0.05\,E_s$). That is

to say that the bigger K_w, the smaller will be the influence of λ. Only when the filling material is missing, $K_w = 0$, an increase in λ leads to a decrease in ν^*

5. Some practical applications

The high efficiency of the composite structures in nature, like plants stems and parenchyma tissues inspired this paper. In particular, the parenchyma is a plant tissue composed by thin-walled polyhedral cells filled by a quasi-incompressible fluid that exerts the hydrostatic pressure P_i (known as turgor pressure) on the cell walls and is responsible for the strength and rigidity of the cell (Van Liedekerke et al., 2010). It is acknowledged that the mechanical properties of the whole tissue are related to those of the individual components, as the constitutive equations of the cell walls, the turgor pressure and the cell-to-cell interactions (Zhu and Melrose, 2003). However, the physical

Table 5
Young's modulus for apple parenchyma tissue.

	E^* (MPa)
Present	
$h/l = 0.02 \div 0.2$ (by assumption)	1÷1.6
$\ell\, k_w = 0.3 \div 4.1$MPa, $P_i = 0.8$MPa (Georget et al., 2003)	
$E_s = 52.8$MPa (Wu and Pitts, 1999), $\nu_s = 0.24$ (Wu and Pitts, 1999)	
$\ell = 1.5$ μm (Sanchis Gritsch and Murphy, 2005)	
Gibson et al. (2010)	0.31÷3.46

Table 6
Young's modulus for potato parenchyma tissue.

	E^* (MPa)
Present	
$h/\ell = 0.0087, \ell = 1.5\mu m$ (Sanchis Gritsch and Murphy, 2005)	4÷4.2
$\ell\, k_w = 9.6 \div 9.62$MPa, $P_i = 0.8$ MPa (Georget et al., 2003)	
$E_s = 500 \div 600$MPa, $\nu_s = 0.5$ (Niklas, 1992)	
Gibson (2012)	5÷6
$h/\ell = 0.0087, E_s = 500 \div 600$MPa	
Experimental value (Gibson, 2012)	3.5÷5.5

Table 7
Young's modulus for carrot parenchyma tissue, with $E_s = 100$ MPa, $\nu_s = 0.33$.

	E^* (MPa)
Present	
$h/\ell = 0.02 \div 0.2, \ell\, k_w = 0.3 \div 4.1$MPa	1.7÷2
$\ell = 1.5\mu$ m (Sanchis Gritsch and Murphy, 2005)	
$P_i = 0.8$MPa (Georget et al., 2003)	
Gibson, Ashby model (Georget et al., 2003)	2.4÷32.8
$h/\ell = 0.02 \div 0.35$	
Warner, Edwards model (Georget et al., 2003)	Lower limit: $10^{-5} \div 1.6$
$h/\ell = 0.02 \div 0.35$	Upper limit: 0.03÷14.2
Experimental value (Georget et al., 2003)	7 ± 1

properties of the living cells are, in general, very difficult to measure (Wu and Pitts, 1999) and, as a consequence, the analysis of the parenchyma tissue is extremely complex without great simplifications and assumptions.

Applying the results of our model to the parenchyma tissue of carrot, potato and apple is a tool to validate the present modeling approach. Specifically, the expression in (41) gives the Young's modulus of the whole tissue, starting from the experimental measurements of the cell properties, Young's modulus, Poisson's ratio, dimensions of the walls, turgor pressure values, and some considerations (see Appendix C) to obtain an approximation of k_w, the Winkler foundation constant. An approximate value of the length of the carrot, potato and apple parenchyma cell walls derives from (Sanchis Gritsch and Murphy, 2005), where the authors describe the structure of the parenchyma cell at different stages of development. In the present paper, the mature cell is considered. Regarding the value of the turgor pressure, (Georget et al., 2003) obtain its values by focusing on the carrot parenchyma tissue. In our investigation, for simplicity, the assumption of the same turgor pressure value for all the considered parenchyma tissues holds true.

Tables 5–7 show that our results generally agree with the experimental published data and with the predictions of other authors, derived from 3D models of fluid-filled, closed-cell foams. It should be noted that a rigorous examination of the parenchyma tissue is beyond our aim.

However, Tables 5–7 indicate that the proposed theoretical model, based on a 2D configuration, could be a useful tool to gain some quantitative information on the mechanical properties of some vegetative tissues.

6. Conclusions

This paper, inspired by the high efficiency of composite structures in nature, focuses on the analysis of the mechanical behavior of a 2D composite cellular material, having a honeycomb texture and the cells filled by a generic elastic material.

Within the framework of linear elasticity and by modeling the microstructure as a sequence of beams on Winkler elastic foundation, the constitutive equations and elastic moduli in the macroscopic continuum description are derived. Specifically, an energetic approach leads to the continuum representation. The assumption that, in the limit, the variables defined to represent displacements and rotations of the nodes can be expressed in terms of two continuous fields solved the passage from discrete to continuum. Finally, the introduction of the aforementioned continuous fields in the strain energy function of the unit cell and simple mathematical manipulations yield the stress-strain relations and elastic constants. Obviously, the overall properties are related to the microstructure parameters. The analysis developed to investigate such influence,
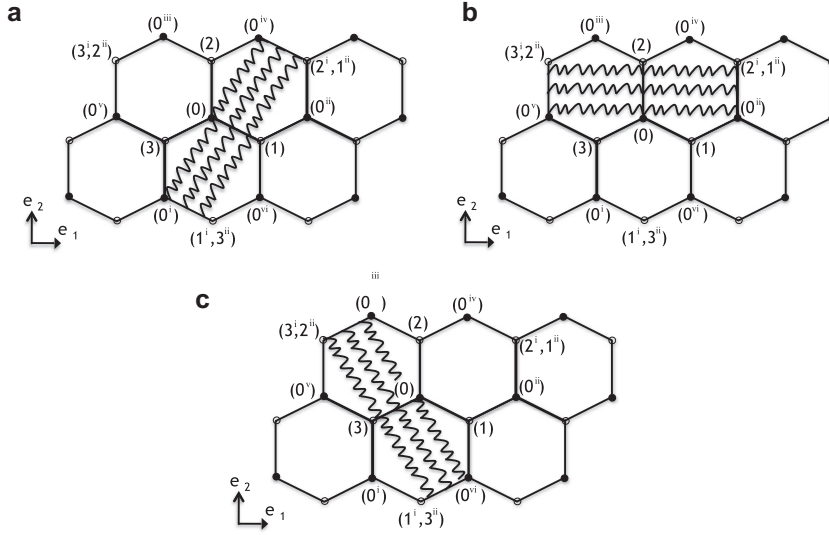
Fig. A1. The triplet of elastic beams with focus on springs. (a) Beam (0)-(1), (b) Beam (0)-(2), (c) Beam (0)-(3).

reveals that the macroscopic mechanical behavior of the medium is improved by increasing the stiffness of the material that fills the cells. Also, from the finite element simulations performed to assess the analytical model, it emerges that the results from the continuum formulation compare reasonably well with the numerical solutions.

In addition, this paper presents the application of the analytical results to the vegetative parenchyma tissue of carrot, apple and potato to derive the Young's modulus of the whole tissue. The values obtained generally agree with the published data and this modeling strategy could provide some qualitative information on the mechanical properties of biological tissues.

To the authors' best knowledge, the beam on Winkler foundation has never been applied to model the microstructure of a cellular material to obtain an analytical expression of the equivalent elastic moduli of a filled cellular solid.

Acknowledgment

Appendix A

The elastic energy of each beam in the discrete system is

$$w^e = \frac{1}{2}(\mathbf{u}^e)^T \cdot \mathbf{k}_b^e \mathbf{u}^e + \frac{1}{2}\left(\frac{1}{2}(\Delta\mathbf{u}^{e,a})^T \cdot \mathbf{k}_{wf}^e \Delta\mathbf{u}^{e,a}\right) + \frac{1}{2}\left(\frac{1}{2}(\Delta\mathbf{u}^{e,b})^T \cdot \mathbf{k}_{wf}^e \Delta\mathbf{u}^{e,b}\right), \tag{1}$$

and, as it can be seen, is the sum of three terms. The first one,

$$\frac{1}{2}(\mathbf{u}^e)^T \cdot \mathbf{k}_b^e \mathbf{u}^e, \tag{2}$$

corresponding to the classical elastic beam, while the second and the third,

$$\frac{1}{2}\left(\frac{1}{2}(\Delta\mathbf{u}^{e,a})^T \cdot \mathbf{k}_{wf}^e \Delta\mathbf{u}^{e,a}\right), \quad \frac{1}{2}\left(\frac{1}{2}(\Delta\mathbf{u}^{e,b})^T \cdot \mathbf{k}_{wf}^e \Delta\mathbf{u}^{e,b}\right), \tag{3}$$

related to the Winkler foundation and, in particular, to the elongation of the springs a, the first, and of the springs b, the second (Fig. A2).

Similarly, the forces and couples acting at the end of each beam are

$$\mathbf{f}^e = \mathbf{k}_b^e \mathbf{u}^e + \mathbf{k}_{wf}^e \Delta\mathbf{u}^{e,a} + \mathbf{k}_{wf}^e \Delta\mathbf{u}^{e,b}. \tag{4}$$

In particular,

$$\Delta\mathbf{u}^{1,a} = \begin{bmatrix} \Delta\mathbf{u}_0^a & \Delta\mathbf{u}_1^a \end{bmatrix}^T, \quad \Delta\mathbf{u}^{2,a} = \begin{bmatrix} \Delta\mathbf{u}_0^a & \Delta\mathbf{u}_2^a \end{bmatrix}^T,$$
$$\Delta\mathbf{u}^{3,a} = \begin{bmatrix} \Delta\mathbf{u}_0^a & \Delta\mathbf{u}_3^a \end{bmatrix}^T \tag{5}$$

and

$$\Delta\mathbf{u}^{1,b} = \begin{bmatrix} \Delta\mathbf{u}_0^b & \Delta\mathbf{u}_1^b \end{bmatrix}^T, \quad \Delta\mathbf{u}^{2,b} = \begin{bmatrix} \Delta\mathbf{u}_0^b & \Delta\mathbf{u}_2^b \end{bmatrix}^T,$$
$$\Delta\mathbf{u}^{3,b} = \begin{bmatrix} \Delta\mathbf{u}_0^b & \Delta\mathbf{u}_3^b \end{bmatrix}^T. \tag{6}$$

The elastic energy of the unit cell, W, derives from that of the three beams it consists of. As stated, adding up forces at the central node (0) and condensing the corresponding degrees of freedom to take account of the forces balance in (0), leads to

$$W = W(\mathbf{u}_1, \mathbf{u}_2, \mathbf{u}_3, \Delta\mathbf{u}_1^a, \Delta\mathbf{u}_2^a, \Delta\mathbf{u}_3^a, \Delta\mathbf{u}_1^b, \Delta\mathbf{u}_2^b, \Delta\mathbf{u}_3^b). \tag{7}$$

The assumption that in the limit $\ell \to 0$ the discrete variables $(\mathbf{u}_j, \varphi_j)$ can be written as

$$\mathbf{u}_j = \hat{\mathbf{u}}_0 + \nabla\hat{\mathbf{u}}\,\mathbf{b}_j$$
$$\varphi_j = \hat{\varphi}_0 + \nabla\hat{\varphi}\,\mathbf{b}_j, \quad j = 1, 2, 3, \tag{8}$$
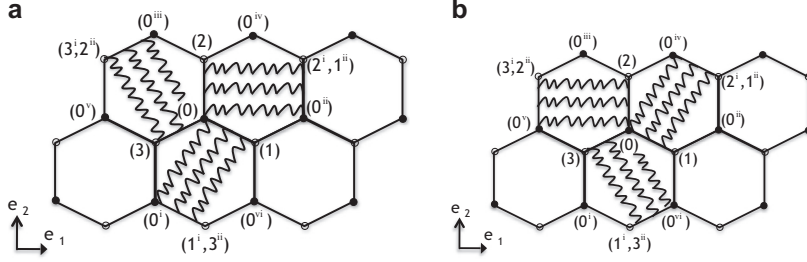
Fig. A2. The two sets of springs connecting the triplet of elastic beams. (a) Springs a, (b) Springs b.
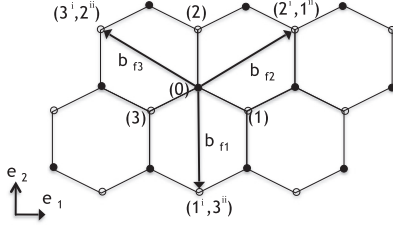

Fig. A3. The $\mathbf{b}_{fi}$ vectors.

provides the continuum description of the discrete structure. The terms $\hat{\mathbf{u}}_0$ and $\hat{\varphi}_0$ are the values of $\hat{\mathbf{u}}(\cdot)$ and $\hat{\varphi}(\cdot)$ at the central point of the cell in the continuum description. Note that in what follows, to simplify the notation, $\hat{\mathbf{u}}$ and $\hat{\varphi}$ stand for $\hat{\mathbf{u}}_0$ and $\hat{\varphi}_0$. Substituting (8) into (7) gives the strain energy of the unit cell as a function of the fields $\hat{\mathbf{u}}$ and $\hat{\varphi}$.

Specifically, the aforementioned quantities are (Figs. A1 and A3):

- Beam (0)-(1)
 Discrete system

$$\Delta \mathbf{u}_1^a = \begin{bmatrix} \mathbf{u}_1 - \mathbf{u}_{1i} \\ \varphi_1 - \varphi_{1i} \end{bmatrix}, \quad \Delta \mathbf{u}_1^b = \begin{bmatrix} \mathbf{u}_1 - \mathbf{u}_{1ii} \\ \varphi_1 - \varphi_{1ii} \end{bmatrix}. \tag{9}$$

In the continuum description,

$$\begin{aligned}
\mathbf{u}_1 &= \hat{\mathbf{u}} + \nabla\hat{\mathbf{u}}\,\mathbf{b}_1, & \varphi_1 &= \hat{\varphi} + \nabla\hat{\varphi}\,\mathbf{b}_1, \\
\mathbf{u}_{1i} &= \hat{\mathbf{u}} + \nabla\hat{\mathbf{u}}\,\mathbf{b}_{f1}, & \varphi_{1i} &= \hat{\varphi} + \nabla\hat{\varphi}\,\mathbf{b}_{f1}, \\
\mathbf{u}_{1ii} &= \hat{\mathbf{u}} + \nabla\hat{\mathbf{u}}\,\mathbf{b}_{f2}, & \varphi_{1ii} &= \hat{\varphi} + \nabla\hat{\varphi}\,\mathbf{b}_{f2},
\end{aligned} \tag{10}$$

that, substituted in (9), lead to

$$\Delta \mathbf{u}_1^a = \begin{bmatrix} \nabla\hat{\mathbf{u}}\,\mathbf{b}_1 - \nabla\hat{\mathbf{u}}\,\mathbf{b}_{f1} \\ \nabla\hat{\varphi}\,\mathbf{b}_1 - \nabla\hat{\varphi}\,\mathbf{b}_{f1} \end{bmatrix}, \quad \Delta \mathbf{u}_1^b = \begin{bmatrix} \nabla\hat{\mathbf{u}}\,\mathbf{b}_1 - \nabla\hat{\mathbf{u}}\,\mathbf{b}_{f2} \\ \nabla\hat{\varphi}\,\mathbf{b}_1 - \nabla\hat{\varphi}\,\mathbf{b}_{f2} \end{bmatrix}. \tag{11}$$

- Beam (0)-(2)
 Discrete system

$$\Delta \mathbf{u}_2^a = \begin{bmatrix} \mathbf{u}_2 - \mathbf{u}_{2i} \\ \varphi_2 - \varphi_{2i} \end{bmatrix}, \quad \Delta \mathbf{u}_2^b = \begin{bmatrix} \mathbf{u}_2 - \mathbf{u}_{2ii} \\ \varphi_2 - \varphi_{2ii} \end{bmatrix}. \tag{12}$$

Continuum description

$$\begin{aligned}
\mathbf{u}_2 &= \hat{\mathbf{u}} + \nabla\hat{\mathbf{u}}\,\mathbf{b}_2, & \varphi_2 &= \hat{\varphi} + \nabla\hat{\varphi}\,\mathbf{b}_2, \\
\mathbf{u}_{2i} &= \hat{\mathbf{u}} + \nabla\hat{\mathbf{u}}\,\mathbf{b}_{f2}, & \varphi_{2i} &= \hat{\varphi} + \nabla\hat{\varphi}\,\mathbf{b}_{f2}, \\
\mathbf{u}_{2ii} &= \hat{\mathbf{u}} + \nabla\hat{\mathbf{u}}\,\mathbf{b}_{f3}, & \varphi_{2ii} &= \hat{\varphi} + \nabla\hat{\varphi}\,\mathbf{b}_{f3},
\end{aligned} \tag{13}$$

and

$$\Delta \mathbf{u}_2^a = \begin{bmatrix} \nabla\hat{\mathbf{u}}\,\mathbf{b}_2 - \nabla\hat{\mathbf{u}}\,\mathbf{b}_{f2} \\ \nabla\hat{\varphi}\,\mathbf{b}_2 - \nabla\hat{\varphi}\,\mathbf{b}_{f2} \end{bmatrix}, \quad \Delta \mathbf{u}_2^b = \begin{bmatrix} \nabla\hat{\mathbf{u}}\,\mathbf{b}_2 - \nabla\hat{\mathbf{u}}\,\mathbf{b}_{f3} \\ \nabla\hat{\varphi}\,\mathbf{b}_2 - \nabla\hat{\varphi}\,\mathbf{b}_{f3} \end{bmatrix}. \tag{14}$$

- Beam (0)-(3)
 Discrete system

$$\Delta \mathbf{u}_3^a = \begin{bmatrix} \mathbf{u}_3 - \mathbf{u}_{3i} \\ \varphi_3 - \varphi_{3i} \end{bmatrix}, \quad \Delta \mathbf{u}_3^b = \begin{bmatrix} \mathbf{u}_3 - \mathbf{u}_{3ii} \\ \varphi_3 - \varphi_{3ii} \end{bmatrix}. \tag{15}$$

Continuum description

$$\begin{aligned}
\mathbf{u}_3 &= \hat{\mathbf{u}} + \nabla\hat{\mathbf{u}}\,\mathbf{b}_3, & \varphi_3 &= \hat{\varphi} + \nabla\hat{\varphi}\,\mathbf{b}_3, \\
\mathbf{u}_{3i} &= \hat{\mathbf{u}} + \nabla\hat{\mathbf{u}}\,\mathbf{b}_{f3}, & \varphi_{3i} &= \hat{\varphi} + \nabla\hat{\varphi}\,\mathbf{b}_{f3}, \\
\mathbf{u}_{3ii} &= \hat{\mathbf{u}} + \nabla\hat{\mathbf{u}}\,\mathbf{b}_{f1}, & \varphi_{3ii} &= \hat{\varphi} + \nabla\hat{\varphi}\,\mathbf{b}_{f1},
\end{aligned} \tag{16}$$

and

$$\Delta \mathbf{u}_3^a = \begin{bmatrix} \nabla\hat{\mathbf{u}}\,\mathbf{b}_3 - \nabla\hat{\mathbf{u}}\,\mathbf{b}_{f3} \\ \nabla\hat{\varphi}\,\mathbf{b}_3 - \nabla\hat{\varphi}\,\mathbf{b}_{f3} \end{bmatrix}, \quad \Delta \mathbf{u}_3^b = \begin{bmatrix} \nabla\hat{\mathbf{u}}\,\mathbf{b}_3 - \nabla\hat{\mathbf{u}}\,\mathbf{b}_{f1} \\ \nabla\hat{\varphi}\,\mathbf{b}_3 - \nabla\hat{\varphi}\,\mathbf{b}_{f1} \end{bmatrix}. \tag{17}$$

Finally, the vectors $\mathbf{b}_{fi}$ (Fig. A3) are

$$\begin{aligned}
\mathbf{b}_{f1} &= -\mathbf{l}_2 + (\mathbf{l}_1 - \mathbf{s}), \\
\mathbf{b}_{f2} &= \mathbf{l}_1 + (\mathbf{l}_2 - \mathbf{s}), \\
\mathbf{b}_{f3} &= (\mathbf{l}_2 - \mathbf{l}_1) - \mathbf{s}.
\end{aligned} \tag{18}$$

Appendix B

Let $\mathbf{U}^e = (\mathbf{U}_I, \mathbf{U}_J)^T = (U_I, V_I, \varphi_I, U_J, V_J, \varphi_J)^T$ be the *vector of nodal displacement expressed in the global reference* and

$$\begin{aligned}
\Delta \mathbf{U}^{e,a} &= \left(\Delta \mathbf{U}_I^a, \Delta \mathbf{U}_J^a \right)^T \\
&= \left(\Delta U_I^a, \Delta V_I^a, \Delta \varphi_I^a, \Delta U_J^a, \Delta V_J^a, \Delta \varphi_J^a \right)^T,
\end{aligned} \tag{19}$$

$$\begin{aligned}
\Delta \mathbf{U}^{e,b} &= \left(\Delta \mathbf{U}_I^b, \Delta \mathbf{U}_J^b \right)^T \\
&= \left(\Delta U_I^b, \Delta V_I^b, \Delta \varphi_I^b, \Delta U_J^b, \Delta V_J^b, \Delta \varphi_J^b \right)^T,
\end{aligned} \tag{20}$$

the elongation of the springs a, the first, and of the springs b, the second. One can prove that the relations

$$\mathbf{u}^e = \mathbf{Q}^e\,\mathbf{U}^e, \quad \Delta \mathbf{u}^{e,a} = \mathbf{Q}^e\,\Delta \mathbf{U}^{e,a}, \quad \Delta \mathbf{u}^{e,b} = \mathbf{Q}^e\,\Delta \mathbf{U}^{e,b} \tag{21}$$

hold true, with $\mathbf{Q}^e$ the *rotation matrix* that rotates the axis $\mathbf{e}_1$, $\mathbf{e}_2$ in η_1^e, η_2^e, given by

$$\mathbf{Q}^e = \begin{bmatrix}
\eta_1^e \cdot \mathbf{e}_1 & \eta_1^e \cdot \mathbf{e}_2 & 0 & 0 & 0 & 0 \\
\eta_2^e \cdot \mathbf{e}_1 & \eta_2^e \cdot \mathbf{e}_2 & 0 & 0 & 0 & 0 \\
0 & 0 & 1 & 0 & 0 & 0 \\
0 & 0 & 0 & \eta_1^e \cdot \mathbf{e}_1 & \eta_1^e \cdot \mathbf{e}_2 & 0 \\
0 & 0 & 0 & \eta_2^e \cdot \mathbf{e}_1 & \eta_2^e \cdot \mathbf{e}_2 & 0 \\
0 & 0 & 0 & 0 & 0 & 1
\end{bmatrix}, \tag{22}$$

$\mathbf{u}^e = [\mathbf{u}_i, \mathbf{u}_j]^T = [u_i, v_i, \varphi_i, u_j, v_j, \varphi_j]^T$ the generalized *vector of nodal displacement expressed in the local reference*,
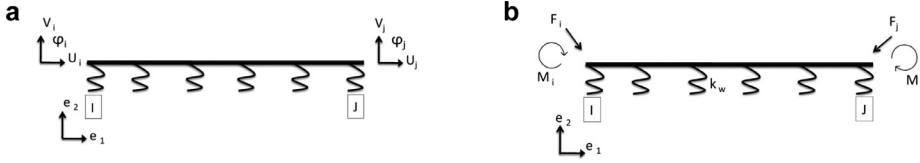
Fig. A4. (a) Degrees of freedom in the global reference system, (b) Forces and couples in the global reference. .
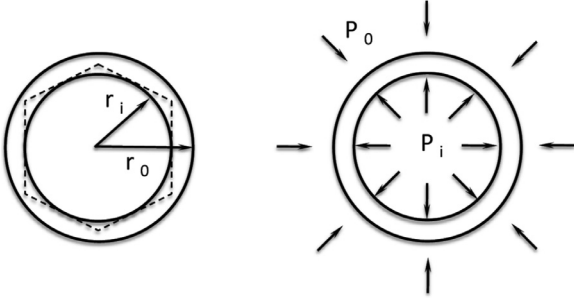

Fig. A5. The internal and external pressures in a parenchyma cell.

$$\Delta \mathbf{u}^{e,a} = \left[\Delta \mathbf{u}_i^a, \Delta \mathbf{u}_j^a \right]^T$$
$$= \left[\Delta u_i^a, \Delta v_i^a, \Delta \varphi_i^a, \Delta u_j^a, \Delta v_j^a, \Delta \varphi_j^a \right]^T, \tag{23}$$

$$\Delta \mathbf{u}^{e,b} = \left[\Delta \mathbf{u}_i^b, \Delta \mathbf{u}_j^b \right]^T$$
$$= \left[\Delta u_i^b, \Delta v_i^b, \Delta \varphi_i^b, \Delta u_j^b, \Delta v_j^b, \Delta \varphi_j^b \right]^T \tag{24}$$

the elongation of the springs a, the first, and of the springs b, the second. Similarly, the *stiffness matrices expressed in the global reference* $\mathbf{K}_b^e$ and $\mathbf{K}_{wf}^e$, can be easily derived by the *stiffness matrices expressed in the local reference*, $\mathbf{k}_b^e$ and $\mathbf{k}_{wf}^e$:

$$\mathbf{K}_b^e = (\mathbf{Q}^e)^T \mathbf{k}_b^e \mathbf{Q}^e, \qquad \mathbf{K}_{wf}^e = (\mathbf{Q}^e)^T \mathbf{k}_{wf}^e \mathbf{Q}^e. \tag{25}$$

Furthermore, the elastic energy in (1) takes the form

$$W^e = \frac{1}{2}(\mathbf{U}^e)^T \cdot \mathbf{K}_b^e \mathbf{U}^e + \frac{1}{2}\left(\frac{1}{2}(\Delta \mathbf{U}^{e,a})^T \cdot \mathbf{K}_{wf}^e \Delta \mathbf{U}^{e,a} \right)$$
$$+ \frac{1}{2}\left(\frac{1}{2}(\Delta \mathbf{U}^{e,b})^T \cdot \mathbf{K}_{wf}^e \Delta \mathbf{U}^{e,b} \right), \tag{26}$$

if referred to the global reference.

As regards the forces and couples acting at the ends of each beam (Fig. A4b), in the global reference are

$$\mathbf{F}^e = \mathbf{K}_b^e \mathbf{U}^e + \mathbf{K}_{wf}^e \Delta \mathbf{U}^{e,a} + \mathbf{K}_{wf}^e \Delta \mathbf{U}^{e,b}, \tag{27}$$

been $\mathbf{F}^e = [\mathbf{F}_I, \mathbf{F}_J]^T = [F_{XI}, F_{YI}, M_I, F_{XJ}, F_{YJ}, M_J]^T$ the *vector of nodal forces and couples expressed in the global reference*, $\mathbf{U}^e$, $\Delta \mathbf{U}^{e,\,a}$, $\Delta \mathbf{U}^{e,\,b}$, $\mathbf{K}_b^e$ and $\mathbf{K}_{wf}^e$ the quantities previously defined.

Appendix C

A sequence of beams on Winkler elastic foundation simulates the microstructure of the composite material analyzed in the present paper.

Focusing on a generic parenchyma cell provides a suitable approximation of K_w, the Winkler's foundation constant. Specifically, a parenchyma cell can be modeled

(Niklas, 1989) like a cylinder of length L with inner radius r_i and outer radius r_o. Every cell is filled by a fluid that exerts the hydrostatic pressure P_i, turgor pressure, on the cell walls (Fig. A5).

Restricting the analysis to the 2D space, a circular thin-walled flexible ring stiffened by the internal pressure P_i can represent the parenchyma cell. Furthermore, when the external pressure P_o exceeds the internal pressure P_i, the flexible ring fails through elastic instability. At the onset of buckling, $P_o = P_i$, the flexible ring behaves as a fictitious stiff ring whose critical buckling load is

$$P_{cr} = \left(\frac{3 E_w I}{r_i^3} \right) \frac{1}{\ell} = P_i, \tag{28}$$

been E_w and $I = \pi (r_o^4 - r_i^4)/4$, respectively, the Young's modulus of the cell walls of the stiff ring and the moment of inertia of the cross section.

From (28), the fictitious Young's modulus is

$$E_w(P_i) = \frac{P_i r_i^3 \ell}{3 I}. \tag{29}$$

A 2D parenchyma cell can also be represented as a composite material. That is, as a stiffened thin-walled cell filled by an elastic material having Young's modulus E_f. From the rule of mixtures,

$$E^{eq} = E_f f + E_s (1 - f), \tag{30}$$

been E^{eq} and E_s, respectively, the Young's modulus of the composite structure and of the cell walls, f the porosity given by

$$f = \frac{V_f}{V_f + V_s}. \tag{31}$$

Also, V_s and V_f stand, in turn, for the volume of the walls and of the material within the cell. In the case of cell thickness tending to zero $V_s \ll V_f$. Accordingly, $f \approx 1$ and

$$E^{eq} = E_f. \tag{32}$$

Furthermore, the equivalence between the biphasic continuum and the hybrid system continuum-spring of Section 2, provide

$$E_f = \frac{5\sqrt{3}}{8} K_w, \tag{33}$$

with K_w the stiffness of the filling material if modeled by a Winkler foundation. Substituting (33) into (32) and imposing the equivalence between the Young's modulus derived from the two modeling strategies, E^{eq} and E_w, provides

$$K_w = \frac{8 P_i r_i^3 \ell}{15\sqrt{3} I}. \tag{34}$$

Note that the relation in (29) is obtained in the case of cylindrical cell. Consequently, to correctly apply (29) to our
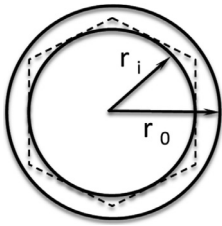
Fig. A6. The annulus approximating the hexagonal cell.

model, it is necessary to approximate the hexagonal cell of the present paper with an annulus. Specifically, the annulus (Fig. A6) has inner and outer radii given, respectively, by $r_i = \sqrt{3}\ell/2$ and $r_o = \sqrt{3}\ell/2 + h$, where ℓ is the length and h the thickness of the beams in the original model.

References

Altenbach, H., Oechsner, A., 2010. Cellular and Porous Materials in Structures and Processes. CISM.

Alzebdeh, K., Ostoja-Starzewski, M., 1999. On a spring-network model and effective elastic moduli of granular materals. J. Appl. Mech. 66, 172–180.

Bruce, D.M., 2003. Mathematical modelling of the cellular machanics of plants. Phil. Trans. R. Soc. Lond. B 358, 1437–1444.

Burlayenko, V.N., Sadowski, T., 2010. Effective elastic properties of foam-filled honeycomb cores of sandwich panels. Compos. Struct. 92, 2890–2900.

Caillerie, D., Mourad, A., Raoult, A., 2006. Discrete homogenization in graphene sheet modeling. J. Elast. 84, 33–68.

Chen, J.Y., Huang, Y., Ortiz, M., 1998. Fracture analysis of cellular materials: a strain gradient model. J. Mech. Phys. Solids 46 (5), 789–828.

Chen, Q., Pugno, N.M., 2011. A parametrical analysis on the elastic anisotropy of woven hierarchical tissues. Adv. Biomater. 13 (10), 337–394.

Chen, Q., Pugno, N.M., 2012. In-plane elastic buckling of hierarchical honeycomb materials. Eur. J. Mech. A/Solids 34, 120–129.

Civalek, O., 2007. Nonlinear analysis of thin rectangular plates on Winkler–Pasternak elastic foundations by DSC–HDQ methods. Appl. Math. Model. 31, 606–624.

Davini, C., Ongaro, F., 2011. A homogenized model for honeycomb cellular materials. J. Elast. 104, 205–226.

Dawson, M.A., Gibson, L.J., 2007. Optimization of cylindrical shells with compliant cores. Int. J. Solids Struct. 44, 1145–1160.

D'Mello, R.J., Waas, A.M., 2013. Inplane crush response and energy absorption of circular cell honeycomb filled with elastomer. Compos. Struct. 106, 491–501.

Dos Reis, F., Ganghoffer, J.F., 2012. Construction of micropolar continua from the asymptotic homogenization of beam lattices. Comput. Struct. 112-113, 354–363.

Eremeyev, V.A., Lebedev, L.P., Altenbach, H., 2013. Foundations of Micropolar Mechanics. Springer.

Fratzl, P., Weinkamer, R., 2007. Natures hierarchical materials,. Prog. Mater. Sci. 52, 1263–1334.

Fratzl, P., Weinkamer, R., 2011. Mechanical adaptation of biological materials - the examples of bone and wood. Mat. Sci. Eng.: C 31, 1164–1173.

Georget, D.M.R., Smith, A.C., Waldron, K.W., 2003. Modelling of carrot tissue as a fluid-filled foam. J. Mater. Sci. 38, 1933–1938.

Gibson, L.J., 1989. Modelling the mechanical behavior of cellular materials. Mat. Sci. Eng. A110, 1–36.

Gibson, L.J., 2005. Biomechanics of cellular solids. J. Biomech. 38, 377–399.

Gibson, L.J., 2012. The hierarchical structure and mechanics of plant materials,. J. R. Soc. Interface 9, 2749–2766.

Gibson, L.J., Ashby, M.F., 2001. Cellular Solids. Structure and Properties. Cambridge University Press.

Gibson, L.J., Ashby, M.F., Harley, B.A., 2010. Cellular Materials in Nature and Medicine. Cambridge University Press.

Gibson, L.J., Ashby, M.F., Schajer, G.S., Robertson, C.I., 1982. The mechanics of two-dimensional cellular materials. Proc. R. Soc. Lond. A 382, 25–42.

Gonella, S., Ruzzene, M., 2008. Homogenization and equivalent in-plane properties of two-dimensional periodic lattices. Int. J. Solids Struct. 45, 2897–2915.

Gordon, R., Losic, D., Tiffany, M.A., Nagy, S.S., Sterrenburg, F.A.S., 2008. The glass menagerie: diatoms for novel applications in nanotechnology. Trends Biotechnol. 27 (2), 116–127.

Guiducci, L., Fratzl, P., Brechet, Y.J.M., Dunlop, J.W.C., 2014. Pressurized honeycombs as soft-actuators: a theoretical study. J. R. Soc. Interface 11 (98).

Janco, R., 2010. Solution methods for beam and frames on elastic foundation using the finite element method. In: Proceedings of Mechanical Structures and Foundation Engineering, International Scientific Conference MSFE.

Kerr, A.B., 1964. Elastic and viscoelastic foundation models. J. Appl. Mech. 31, 491–498.

Kumar, R.S., McDowell, D.L., 2004. Generalized continuum modeling of 2-d periodic cellular solids. Int. J. Solids Struct. 41, 7399–7422.

Limkatanyu, S., Ponbunyanon, P., Prachasaree, W., Kuntiyawichai, K., Kwon, M., 2014. Correlation between beam on winkler-pasternak foundation and beam on elastic substrate medium with inclusion of microstructure and surface effects. J. Mech. Sci. Technol. 28, 3653–3665.

Murray, G., Gandhi, F., Hayden, E., 2009. Polymer filled honeycombs to achieve a structural material with appreciable damping. Am. Instit. Aeronaut. Astronaut..

Neethirajan, S., Gordon, R., Wang, L., 2009. Potential of silica bodies (phytoliths) for nanotechnology. Trends Biotechnol. 27 (8), 461–467.

Niklas, K.J., 1989. Mechanical behavior of plant tissues as inferred from the theory of pressurized cellular solids. Am. J. Bot. 76 (6), 929–937.

Niklas, K.J., 1992. Plant Biomechanics: An Engineering Approach to Plant Form and Function. University of Chicago Press.

Ostoja-Starzewski, M., 2002. Lattice models in micromechanics. Appl. Mech. Rev. 55 (6), 35–60.

Pugno, N.M., 2006. Mimicking nacre with super-nanotubes for producing optimized super-composites. Nanotechnology 17, 5480–5484.

Sanchis Gritsch, C., Murphy, R.J., 2005. Ultrastructure of fibre and parenchyma cell walls during early stages of culm development in dendrocalamus asper. Ann. Bot. 95, 619–629.

Van Liedekerke, P., Ghysels, P., Tijskens, E., Samaey, G., Smeedts, B., Roose, D., Ramon, H., 2010. A particle-based model to simulate the micromechanics of single-plant parenchyma cells and aggregates. Phys. Biol. 7.

Wang, X.L., Stronge, W.J., 1999. Micropolar theory of two-dimensional stresses in elastic honeycomb. Proc. R. Soc. Lond. A 455, 2091–2116.

Warner, M., Thiel, B.L., Donald, A.M., 2000. The elasticity and failure of fluid-filled cellular solids: theory and experiment,. PNAS 97 (4), 1370–1375.

Warren, W.E., Byskov, E., 2002. Three-fold symmetry restrictions on two-dimensional micropolar materials,. Eur. J. Mech. A/Solids 21, 779–792.

Wu, N., Pitts, M.J., 1999. Development and validation of a finite element model of an apple fruit cell. Postharvest Biol. Tec. 16, 1–8.

Zhu, H.X., Melrose, J.R., 2003. A mechanics model for the compression of plant and vegetative tissues,. J. theor. Biol. 221, 89–101.